# Predicting Personalised Therapeutic Combinations in Non-Small Cell Lung Cancer Using In Silico Modelling

Matthew A. Clarke[1^], Charlie George Barker[1^], Ashley Nicholls[2^], Matt P. Handler[1], Lisa Pickard[3], Amna Shah[4], David Walter[5], Etienne De Braekeleer[6], Udai Banerji[3], Jyoti Choudhary[3], Saif Ahmed[2], Ultan McDermott[4], Gregory J. Hannon[2*] and Jasmin Fisher[1*]

[1] UCL Cancer Institute, University College London, 72 Huntley Street, London, WC1E 6DD, UK
[2] Cancer Research UK Cambridge Institute, University of Cambridge, Cambridge, CB2 0RE, UK
[3] The Institute of Cancer Research, 123 Old Brompton Road, London, SW7 3RP, UK
[4] AstraZeneca, Oncology R&D, 1 Francis Crick Avenue, Cambridge, CB2 0AA, UK
[5] Cancer Research Horizons, Cambridge, CB2 0RE, UK
[6] AstraZeneca, Discovery Science R&D, 1 Francis Crick Avenue, Cambridge, CB2 0AA, UK

^These authors contributed equally to this work

*Correspondence should be addressed to Gregory Hannon greg.hannon@cruk.cam.ac.uk or Jasmin Fisher jasmin.fisher@ucl.ac.uk

## Abstract

The disease burden from non-small cell lung cancer (NSCLC) adenocarcinoma is substantial, with around a million new cases diagnosed globally each year, and a 5-year survival rate of less than 20%. A lack of therapeutic options personalized to individual patient genetics, and the targeted therapies that exist quickly succumbing to resistance, leads to high variation in survival. Patient stratification combined with greater personalisation of therapies have the potential to improve outcomes, however, the wide variation in mutations found in NSCLC adenocarcinoma patients mean that experimentally determining suitable treatment combinations is time-consuming and expensive. Here we present an *in silico* model encompassing tumour intrinsic key oncogenic signalling pathways, including EGFR, AKT, JAK/STAT and WNT for efficiently predicting rational drug-drug and drug-radiotherapy combination therapies in NSCLC. Using this model, we simulate diverse genetic profiles and test over 10,000 therapeutic combinations to identify optimal strategies to overcome resistance mechanisms specific to genetic profiles and p53 status. Our *in silico* model reproduces drug additivity experiments, predicts radio-sensitising genes validated in a CRISPR screen and identifies 53BP1 as a potential drug target that improves the therapeutic window during radiotherapy, as well as potential to use ATM inhibitors to overcome p53 loss-of-function driven radiotherapy resistance. We further use the *in silico* model to identify a 19-gene signature to stratify patients most likely to benefit from radiotherapy and validated this using TCGA data. These results further demonstrate the utility of *in silico* mechanistic modelling and present a bespoke computational resource for large-scale screening of personalised therapies applied to NSCLC.

## Introduction

Lung cancer is the leading cause of cancer-related deaths worldwide, resulting in an estimated 1.8 million deaths annually. Non-small cell lung cancer (NSCLC) adenocarcinoma accounts for ~85% of lung cancer cases and has a 5-year survival rate of 19%[1]. Treatment options have advanced substantially over the last 10 years, with new surgical approaches, chemotherapeutic drugs and better targeted radiotherapy, with patients now often treated with several of these in combination[1,2]. However, overall survival remains low[3], in part because current approaches do not account for the diversity of oncogenic mutations driving NSCLC[4]. Furthermore, in cases where targeted therapy is applicable, resistance is inevitable, with the majority of patients treated with first-generation EGFR inhibitors developing resistance after 6-9 months of treatment[1,5–7]. A lack of understanding of how tumour genetics affect response to therapy, and the mechanisms underlying resistance, limit our ability to rationally design treatments that pre-empt and overcome resistance, and personalise therapeutics to maximise individual patient outcomes[8].

Radiotherapy delivers a high dose of radiation to cancer cells to cause the rapid accumulation of double-stranded breaks (DSBs)[9,10]. If unrepaired, these DSBs trigger cell death[11], while healthy cells are better able to repair these breaks and survive. Radiotherapy has a significantly lower treatment-associated mortality than surgery[12], although the efficacy of surgery is higher than that of radiotherapy in terms of overall survival[13], owing in part to adaptation of the tumour and evolution of radio resistance-associated mutations[14]. Extending the benefits of radiotherapy to more patients and improving efficacy to reduce the chance of resistance emerging requires better understanding of how variation in treatment response is driven by differences in driver mutations. This will allow tailoring of radiotherapy to patient biology by combining it with radio-sensitising treatments.

Recent advances in modelling patient biology as executable computer programs are now beginning to uncover the principles underlying how the genetics of a cancer contributes to its behaviour and the potential mechanisms that give rise to phenotypes such as therapeutic resistance[15–21]. Here, we present a bespoke executable model of NSCLC adenocarcinoma oncogenic signalling that covers key pathways including the cell cycle, apoptosis cascade and DNA damage response (DDR). This model can mechanistically link oncogenic genetics and signalling, by representing biological processes as nodes within a qualitative network, with functions determining the activation of biological components[22]. The model is 'executed' by allowing nodes to interact with each other dynamically, such that the stable state of the network represents the overall cellular phenotype[23]. The model can be used to test combinations of mutations and inhibitors involving proteins that are not yet druggable, allowing identification of potential drug targets for future research and development. It can also be interrogated in greater depth than real systems as every variable and interaction in the model can be controlled individually, allowing for more complete exploration of the mechanisms underpinning observations. Moreover, this mechanistic understanding of how therapy interacts with the oncogenic mutations allows us to identify the genetic determinants of responses to therapy.

Here we use this *in silico* model to explore 136 possible radio-sensitising treatments across a panel of 7 cancer cell lines and explore the effect of specific mutations on treatment sensitivity. Once the model successfully recapitulates previously published sensitivities of different NSCLC adenocarcinoma cell lines to combination drug treatment and radiotherapy, we use the model

to screen ~66,000 combinations to find the optimal therapeutic strategy for a given genotype. We exploit the interpretable nature of our i*n silico* model to understand why these sensitivities occur and how specific mutations determine the NSCLC adenocarcinoma responses to therapy. We then perform *in silico* screens for perturbations that can sensitise cancer cells to radiotherapy while protecting healthy cells, as well as overcome p53-driven radiotherapy resistance. Overall, our platform is a powerful tool for understanding therapeutic responses to treatment in NSCLC. Harnessing the power of executable models will provide a more complete understanding of how genetics contributes to oncogenic signalling and enable therapy to be tailored to the genetics underlying the cancer, improving treatment outcomes for patients.

## Results

### An executable network map of KRAS-, EGFR- and MET- driven NSCLC adenocarcinoma

To understand the contributions of oncogenic mutations in NSCLC adenocarcinoma to drug and radiotherapy response, we built an executable qualitative network model using the BioModelAnalyzer (BMA) tool (https://biomodelanalyzer.org, see Methods) following the workflow outlined in Figure 1A. The model describes the core pathways covering the most common driver mutations in NSCLC patients[24], including EGFR, AKT, JAK/STAT and WNT pathways, as well as commonly overexpressed genes such as MYC and NRF2. We modelled how these mutations drive changes in cell cycle and apoptosis. To model radiotherapy responses, we include the DNA damage repair (DDR) pathways, homologous recombination (HR) and Non-Homologous End Joining (NHEJ).

An extensive literature survey of 171 research papers identified interactions between genes and proteins in NSCLC adenocarcinoma resulting in a model with 160 nodes and 360 edges describing activating regulatory relationships or inhibiting relationships between biological components (Supplementary Table S1). To provide context to these interactions, each node has a corresponding target function defining its activity (Shown in Figure 1B, Supplementary Table S1, S2 and S3). The value describing the activity of nodes is discrete and ranges between 4 levels (0 to 3). A level of 0 indicates loss-of-function and 3 indicates gain-of-function.

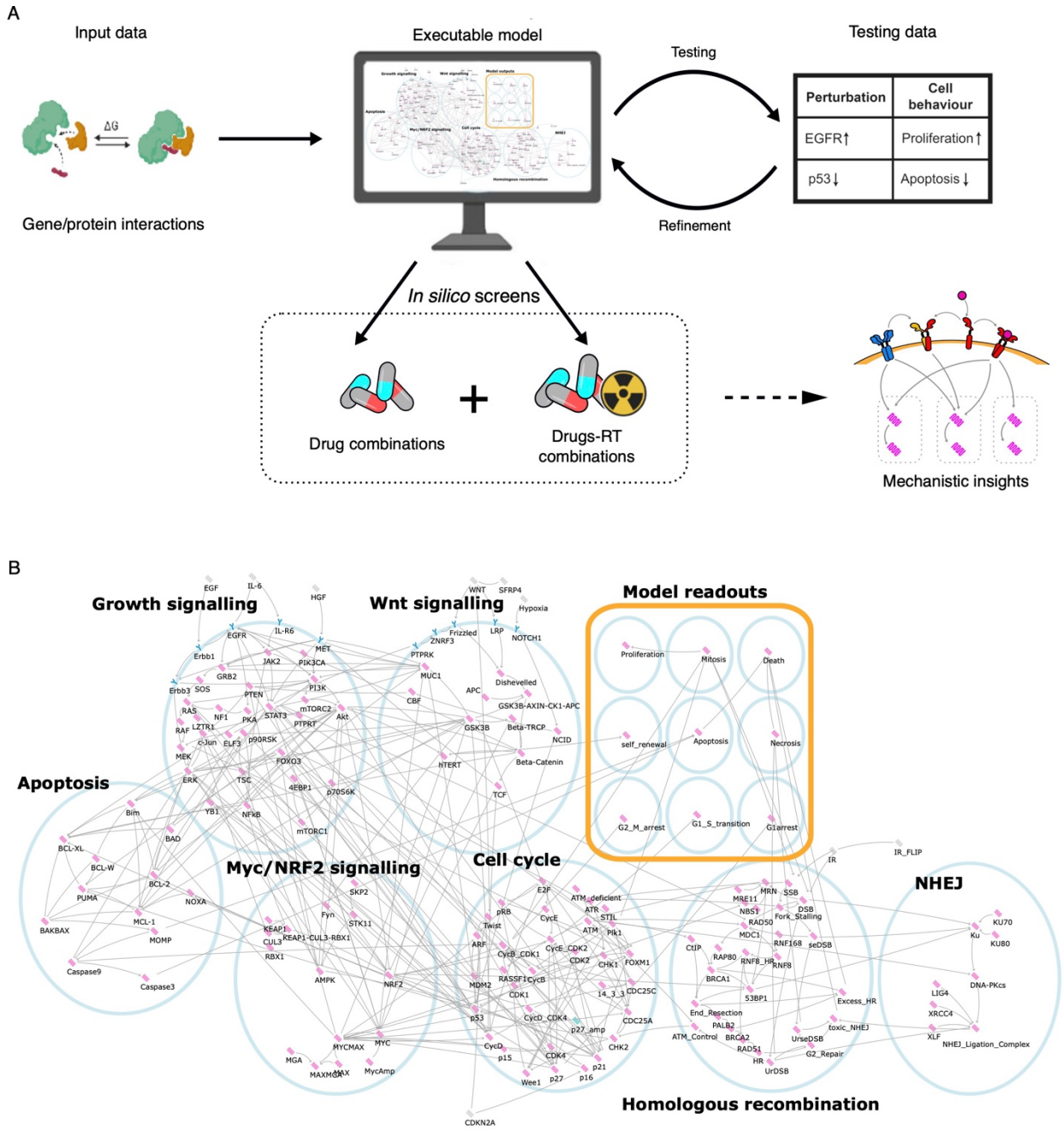


**Figure 1. Outline of the workflow and executable NSCLC adenocarcinoma model. A)** Schematic showing the workflow used to construct, test, and analyse the model. **B)** A network visualising the architecture of the executable model as seen in the BMA tool. Different subnetworks are enclosed by a blue circle, model inputs are coloured grey, receptors are coloured blue and cytosolic proteins are coloured pink. Edges represent regulatory interactions between proteins and are pointed for activating edges (→) and blunt for inhibiting (⊣). The phenotypic readouts are shown enclosed in a yellow box.

## The NSCLC adenocarcinoma network model reproduces experimental data

To train the model, we collated a list of 26 publications reporting the behaviour of NSCLC adenocarcinoma cell lines under different experimental conditions, separate from and not used to build the model. These publications describe the behaviours (e.g., growth rates, levels of

167 apoptosis, protein levels) of different cell lines under perturbation by drugs and/or radiation. Cell
168 lines were modelled by setting the nodes that represent genes with known driver mutations to
169 the appropriate constant value (0 for loss-of-function and 3 for gain-of-function). Cell line
170 mutation data were drawn from Cell Model Passports[25] and our own experiments (see Methods,
171 Supplementary Table S4 and Supplementary Figure S1). We then used the model to find the
172 stable states of the system, which we compared to the phenotypes measured in the experiments.
173 Comparison of the simulated behaviours with the published observations was used to iteratively
174 improve the target functions of the nodes within the model until the model recapitulates the
175 behaviours observed in the published experiments (see Methods, Supplementary Table S5). We
176 also modelled the sensitivity of six cell lines to single drug treatment with and without
177 radiotherapy (HCC44, NCIH1373, NCIH23, NCIH358, NCIH1792, SW1573) and compared to the
178 published literature, to test the DNA-damage repair section of the model (Supplementary Figure
179 S2, S3). We examined common targeted therapies including EGFR[26,27], MEK, MET,[28] and DNA-PK
180 inhibitors[29,30] and further verified that the model reproduced the effects of knock-out
181 experiments on key proteins in oncogenic processes, including KRAS[31–34], MUC1[35], NRF2[36,37],
182 JAK2[38], RAD51[39], ATM[40], RNF8[41], NOTCH1[42] and TP53[32]. When comparing the model behaviour
183 to these published experiments, we see an accuracy of 91% (Supplementary Table S5, See
184 Methods).
185 To identify treatments that maximise the difference, for the same dose, between the effect on
186 cancer and healthy cells (maximise the therapeutic window) we also simulated healthy lung cells.
187 We assume that the signalling processes in these cells are the same as in lung cancer except
188 without driving oncogenic mutations. We tested this assumption by comparing to published
189 experiments conducted using the immortalised epithelial lung cell lines HBEC3 and BEAS-2B[32,43]
190 (Supplementary Table S4). Having reproduced existing experimental data, we next used the
191 model to systematically predict the effect of unseen combinations of knock-outs in our panel of
192 NSCLC adenocarcinoma cell lines.

193 **Targeted monotherapies inhibiting Erbb1, RAS and STAT3 have an effective but narrow**
194 **therapeutic window**

195 To simulate personalised therapies with single targeted drugs, we systematically set the value of
196 95 druggable (see Methods, Supplementary Table S6 and Supplementary Figure S3) nodes in the
197 model to 0 in six NSCLC adenocarcinoma cell lines (SW1573, NCIH1792, HCC827, PC9, A549 and
198 NCIH1993) chosen for a range of driver mutations to reflect the genetic heterogeneity of NSCLC
199 (See Supplementary Figure S1). By setting the value of nodes to a constant value of 0, we mimic
200 the effect of inhibitors that could be used as targeted therapy. Overall, we observed that cancer
201 cells are more resistant to targeted therapy than healthy cells when considering both cell
202 proliferation and death levels (Supplementary Figure S2). Perturbations that are effective at
203 killing cancer cell lines are those that directly target proteins downstream of activated oncogenes
204 specific to those cell lines (e.g., EGFR in HCC827 and PC9 or KRAS in NCIH1993, NCIH1792 and
205 A549), however, these treatments are also lethal to healthy cells. Inhibition of STAT3 kills cells in
206 the A549 and NCIH1993 cell lines (Supplementary Figure S2C), a pattern observed with all other
207 potential treatments demonstrating how small differences in mutational profile can lead to total
208 resistance to therapy.

When identifying potential cytostatic treatments, we identify more potential drug targets. This includes inhibiting MYC, which limits oncogenic growth to the basal growth rate of healthy cells while
also reducing apoptotic signalling in all cell lines profiled apart from A549. In general, we see that healthy cell lines are more susceptible to treatment via the inhibition of single proteins than cancer cells (Supplementary Figure S2C). This underlines the importance of using combination therapies to maximise the perturbation space to find cancer-specific treatment options with a good therapeutic window.

**NRF2 inhibition is predicted to protect healthy cells while 53BP1 inhibition sensitise cancer cells to radiotherapy**

We next sought to assess combining targeted therapy with radiotherapy to see whether this would improve predicted treatment efficacy. We therefore used the model to assess the radio-sensitising effect of gene knockouts and compared the predictions to an *in vitro* CRISPR screen of radiation sensitive and resistant lung adenocarcinoma cell lines (HCC44, NCIH1373, NCIH23, NCIH358, NCIH1792, SW1573). We set one node at a time to a constant value of 0 to mimic a knock-out, in addition to cell line-specific mutations (Supplementary Table S4), and compared this effect with or without radiation, modelled through the value of the 'IR' node, (Supplementary Figure S3). The effect of IR is modelled through the induction of single-strand breaks (SSB), double-strand breaks, and replication-induced or single-ended double strand breaks (seDSB)[44]. We modelled the impact of SSB on fork stalling and collapse, and the subsequent generation of seDSB[45] as well as the downstream repair of DSB and seDSB by homologous recombination and non-homologous end-joining[46], with unrepaired breaks and toxic chromosome fusions leading to increased cell death. We define an effective radio-sensitising knockout as one that leads to more cell death as part of a combination compared to either the gene knockout or radiotherapy alone. We term the additive difference between cell death in the combination treatment and the most effective of these two monotherapies as ‘radio-sensitisation’ (see Figure 2A).
The model predicts broad classes of radio-sensitising knockouts. Some knockouts are radio-sensitising in both healthy and cancer cells; primarily inhibition of the NHEJ pathway, as expected[47]. Other known treatments such as ATM inhibition[48] are radio-sensitising across all cancer cell lines, but we also see cell line-specific radio-sensitising knockouts. For example, 53BP1 inhibition is particularly additive in SW1573 (Figure 2A-B). Such cell line specific behaviour demonstrates the difficulty in maintaining an effective therapeutic window across diverse patient mutations, and underlines the requirement for tailored therapeutic approaches to diverse mutational profiles.

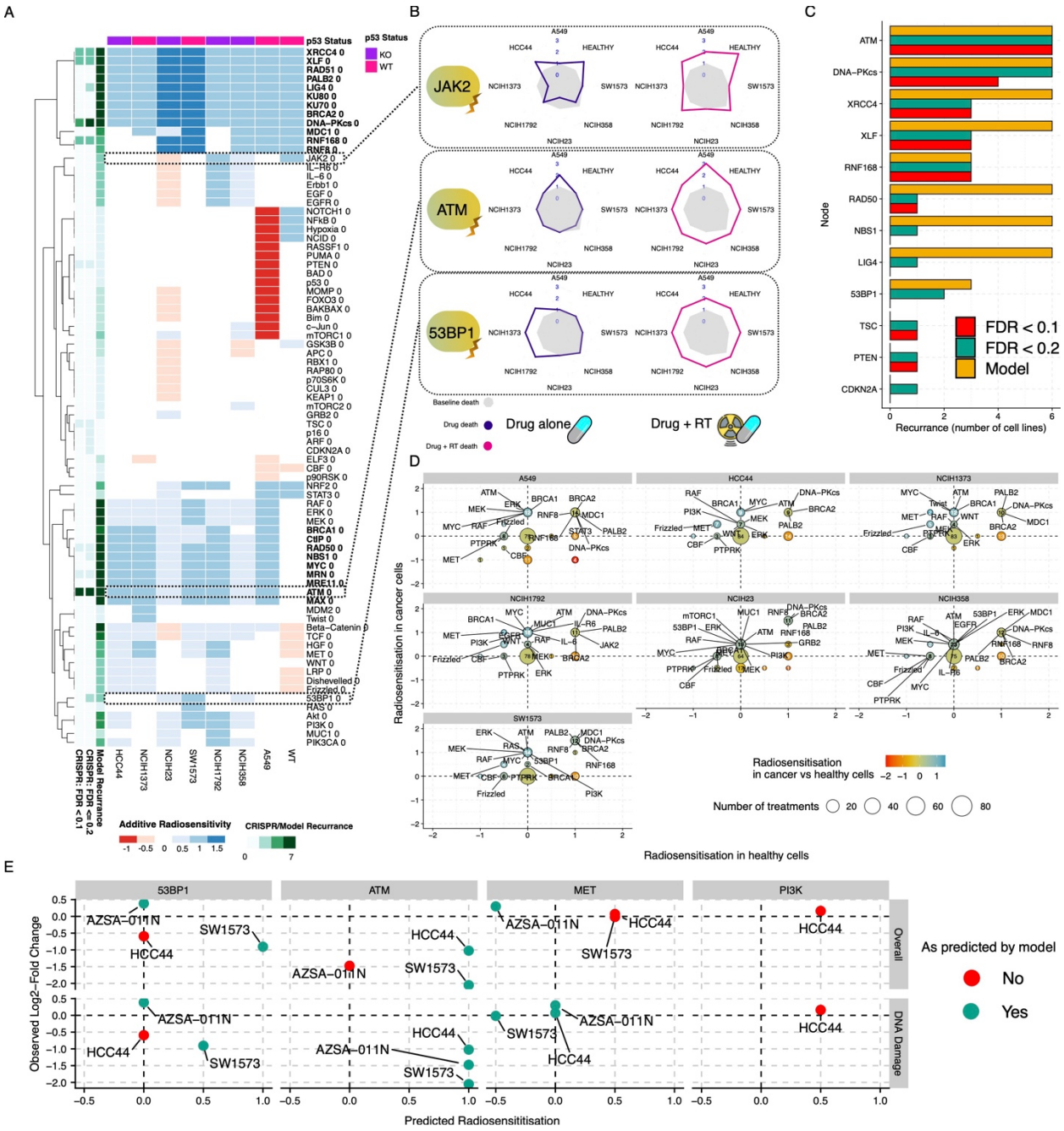


**Figure 2. Systematic screen of perturbations on the *in silico* model reveals inhibition of ATM and 53BP1 as radio-sensitising agents. A)** A heatmap showing predicted radio-sensitising effect *in silico* knockouts (rows, where the node value is set to 0), on NSCLC adenocarcinoma cell lines (columns). Radio-sensitisation is the increase (blue) or decrease (red) in cell death in the combination of IR and knock-out compared to the most effective of IR or knock-out applied alone. Side panels (green) show the number of cell line backgrounds in which the treatment was radio-sensitising in the model or the CRISPR screen (at FDR ≤ 0.2 and < 0.1) where we count a recurrence if radiosensitivity is observed at this threshold for any timepoint in the screen. Knockouts that confer broad radiosensitivity are shown in bold. **B)** Radar plots showing the levels of death after drug treatments (for ATM, 53BP1 and JAK2) (dark blue) and after drug treatment and irradiation (magenta) compared to the baseline (grey). Specific drug combinations that are broadly radio-sensitising across backgrounds are outlined in black in the heatmap in panel A. **C)** Number of cell lines in which knockouts were predicted to be effective in: the network model (yellow), CRISPR screen with FDR ≤ 0.2

(green), or CRISPR screen with FDR < 0.1 (red). Note: p16 and p14ARF knockouts were both observed to be effective in the CRISPR screen. These are both controlled by the CDKN2A node in the model and so are grouped under that node. **D)** X-axis change in healthy cell radio-sensitivity. Y-axis relative change in cancer cell radio-sensitivity. Blue is more radio-sensitisation of cancer than healthy; red is more radio-sensitisation of healthy than cancer. Point size is the number of knockouts that have this effect. **E)** Observed Log2-Fold-Change (y) vs predicted radio-sensitisation for genes in focussed CRISPR screen (x). Values shown are for maximum timepoint. Colour is blue for validation (FDR<0.1 for cases where model predicted sensitisation), red otherwise. AZSA-011N cells are healthy cell organoids. Any genes for which knockout was found to be essential at all timepoints were removed. Top row is predicted radio-sensitisation measured by change on overall cell death (measured by node 'Death'), bottom row is predicted radio-sensitisation measured by DNA-Damage specific cell death (measured by node 'Necrosis').

We compared the model results to an *in vitro* CRISPR screen in the six NSCLC adenocarcinoma lines treated with radiotherapy (HCC44, NCIH1373, NCIH23, NCIH358, NCIH1792, SW1573) (Figure 2C). The model correctly predicts those knockouts that led to radio-sensitisation in the *in vitro* CRISPR screen in 9 out of 12 cases (Figure 2C).

The model suggests that the radio-sensitising effects of knockouts outside of the NHEJ pathway are highly specific to mutational context, as we saw for many monotherapies (Figure 2A). In addition, when radiotherapy is applied, the model predicts similar levels of death in NSCLC adenocarcinoma and healthy cells (Supplementary Figure S3B-C). However, the degree to which a drug radio-sensitises a cell (the difference between the combination of IR and knock-out compared to the most effective of either IR or knock-out applied alone) is often higher in the cancer cells than the healthy cells. In particular, there is a subset of cases where all the death in healthy cells is driven by IR, but the majority of death in the cancer cells is driven by the combined effects therapy and IR. This suggests that by reducing the IR dose we could reduce the death in the healthy cells more than in the cancer cells and widen the therapeutic window. Combined with the personalised nature of radio-sensitisation, this prompted us to query the model for knockouts that lead to the largest change in radio-sensitivity.

Figure 2D shows the predicted additive radio-sensitisation of cancer cells versus healthy cells. Many treatments are predicted to radio-sensitise both cancer and healthy cells, for example those involved in DDR pathways. In the case of radio-sensitisation of cancer cells specifically, we predict that inhibition of MYC is particularly effective and specific. This is partly due to the essential role of MYC in proliferation[49], but also because of the regulation of NBS1 by MYC, which, as part of the MRN complex, plays a key role in coordinating the response to DNA damage.

Conversely, we predict that loss of members of the PTP family (e.g., PTPRT), leads to reduction in radio-sensitivity in healthy cells, protecting them from toxicity, while having no effect on many of the cancer cell lines. This is due to an increase in JAK/STAT signalling, with a concomitant increase in MCL-W that suppresses apoptosis, and NRF2, which aids in repair of radiation induced DNA damage. This has less effect in cancer cells as they have already up-regulated NRF2. We examined death from DNA damage (through the node 'Necrosis') specifically as this may play a greater role in response to different radiotherapy doses than apoptotic death (Supplementary Figure S3D). We predict that inhibition of NRF2 is particularly sensitising to DNA-damage associated death in cancer cells, due to reduction in DNA damage repair[50]. Equally, suppression of the KEAP1/CUL3/RBX1 complex leads to an increase in NRF2 in healthy cells, protecting them, without aiding cancer cells, as these over-express NRF2 via mutant KRAS.

To validate this, we test a selection of these genes, MYC, 53BP1, MET, PI3K and ATM in a focussed CRISPR screen in cancer cell lines (SW1573, A549, HCC44) and healthy cell organoids (AZSA-011N). Of these, MYC was unable to be tested as it proved essential in all cell lines. 53BP1 sensitised cancer cells and not healthy cells, in line with the model's predictions, although it sensitised both SW1573 and A549 relative to healthy cells, where we predicted it would be effective only in A549. ATM sensitised all cancer cell lines, as predicted, as well as healthy cells, which the model did not predict. MET did not show the expected sensitisation of the cancer cells (Figure 2E (top)), nor the protection of healthy cells (AZSA-011N). However, in our model we treat Apoptosis and DNA-damage associated death (Necrosis) separately. When examining the latter, we find that the model's predictions align well with observation in all genes and cell lines, other than for HCC44 in the case of 53BP1 and PI3K (Figure 2E (bottom)), although 53BP1 may be essential for HCC44 (essentiality was detected at early time points but not later timepoints).

**ATM inhibition overcomes radio-resistance conferred by TP53 deficiency**

As a key regulator of DNA damage response which is often mutated in cancer, we wanted to explore the association between TP53 mutational status and radiotherapy response in cancer cell lines. Accordingly, we simulated the cell lines from our radio-sensitisation screen with TP53 activated in cell lines where it has a loss-of-function mutation and inactivated in cell lines where it is competent (Supplementary Table S4). The model predicts that TP53 deficiency reduces death from radiation alone in most cell lines (Figure 3A, Supplementary Figure S4). However, when combined with a radio-sensitising knock-out, there are many potential combinations that are predicted to induce death in cancer cell lines regardless of TP53 activation, overcoming the radio-resistance due to TP53 loss-of-function (orange points on dotted line, Figure 3A).
ATM knock-out is an example of a radio-sensitising perturbation that is effective across all cancer cell lines, irrespective of TP53 mutation status (Figure 3B). Therefore, the model predicts that there is benefit in using radio-sensitising agents targeting those proteins identified in our i*n silico* knock-outs to improve the effect of radiotherapy for patients with a TP53 mutation. We experimentally validated these results by modifying SW1573 and NCIH1373 cell lines *in vitro* to flip the mutational status of TP53 (Figure 3C and Supplementary Figure S4A) Indeed, ATM sensitises cancer cells regardless of p53 status in all cancer cell lines for which this was tested in the focussed CRISPR screen (A549 and SW1573), as predicted.

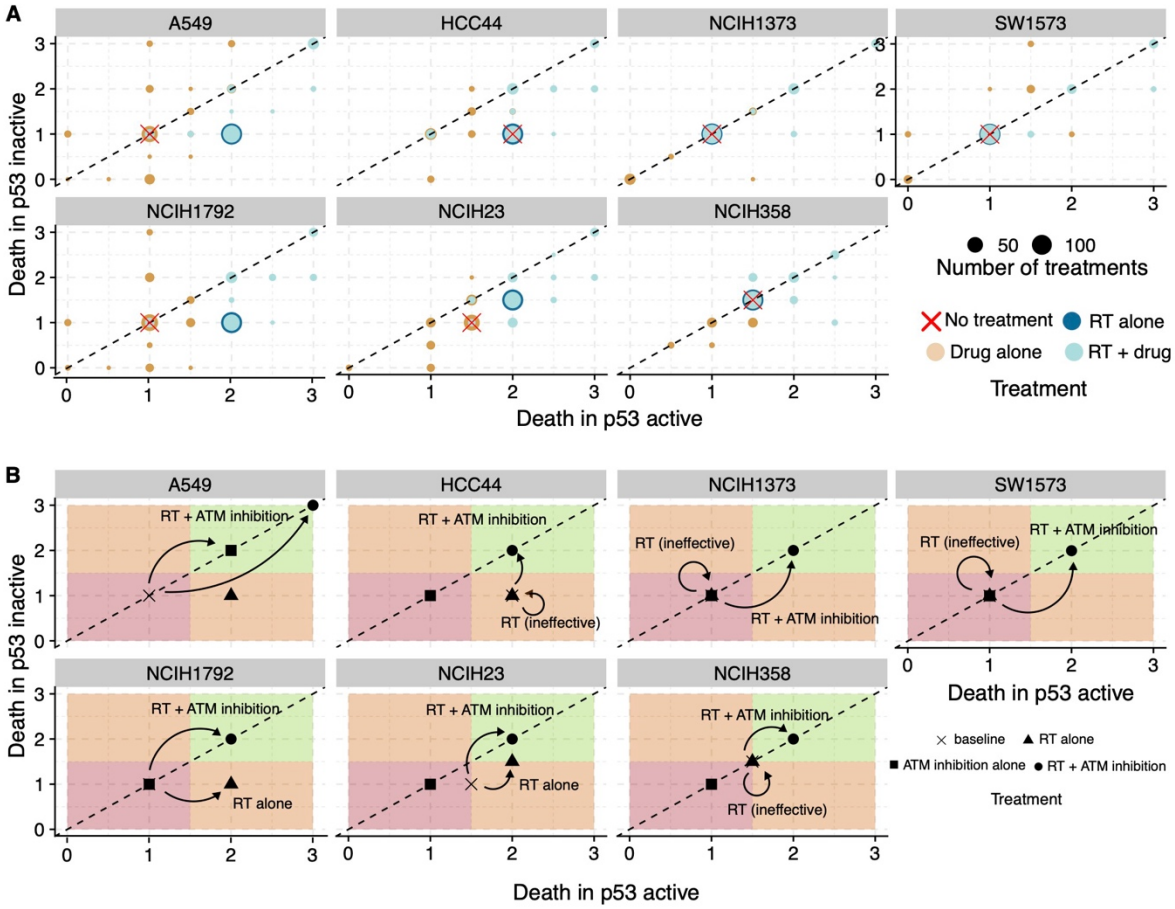


**Figure 3. Radio-sensitising knock-outs increase death in a manner that is agnostic to TP53 status. A)** Levels of death predicted by the models in cell lines that have been modified to have TP53 active (x-axis) and TP53 inactive (y-axis). Colours denote the type of treatment (dark blue for drug treatment alone, light blue for radiotherapy alone and orange for radiotherapy and drug treatment combined) and the size denotes the frequency of treatments in that position. Knock-outs below the dotted line are less effective in TP53 inactive cases then in TP53 active, knock-outs above the dotted line are more effective in TP53-inactive than active. **B)** Death in TP53 deficient (y-axis) and TP53 (x-axis) proficient cell lines showing the differences of radiotherapy alone and radiotherapy with ATM knock-out. Quadrants of the plots are coloured to denote desirable locations for therapeutic outcomes. Green indicates high cancer death regardless of TP53 mutational status, red indicates low death regardless of TP53 mutational status and orange indicates that knock-out efficacy is dependent on TP53 mutational status. Arrows show how in the case of ATM knock-out, the level of cell death with IR moves from below the dotted line i.e., less effective in the TP53 inactive case, to the dotted line, indicating that IR + ATM inhibition overcomes and neutralises the effect of TP53 inactivation.

350 **Predicted radio-sensitising targets stratify patient response to radiotherapy**

351 Following our systematic *in silico* screen of radio-sensitising knockouts, we observed that there
352 was a subset of genes that affect radiation sensitivity agnostic to mutational background. These
353 19 genes are marked in bold on Figure 2 and include members of the DNA damage repair
354 pathways (ATM, MDC1, XRCC6, XRCC4 etc) as well as transcriptional regulators (MYC and MAX).
355 We hypothesised that these candidate genes could be used to stratify patients as either
356 radioresistant or radiosensitive. To explore this, we used the TCGA database
357 (https://www.cancer.gov/tcga) of clinical data to see whether patients with low levels of gene
358 expression (as measured by RNA-seq) or copy number variation (CNV) for our predicted
359 radiosensitive genes survive longer after treatment with radiotherapy. We considered either of
360 these properties to be analogous to the activity of the node within our network model. Patients
361 with both low copy numbers (bottom 5%, n= 76) and of low RNA expression (bottom 10%, n=15)
362 for at least one radio-sensitising gene, compared to all patients, were determined to be
363 radiosensitive (Figure S5A, n=175).
364 When instead considering RNA expression and CNV separately, we found that with either
365 definition of activity of a gene we see a lower hazard ratio (longer survival) for patients predicted
366 to be radiosensitive after receiving radiotherapy (Supplementary Figure S5B-C, Cox proportional
367 hazards regression; HR= 0.4299, P=0.06 for expression and HR= 0.6421, P=0.08 for CNV). When
368 using both CNV and RNA to determine a consensus subset (see Methods) of radiosensitive
369 patients we also see a significant difference in survival (Figure 4A, HR= 0.5842, P=0.03),
370 suggesting that patients with a naturally lower activity of these genes have increased survival.
371 When looking at patients that have not received radiotherapy (n=705, Supplementary Figure
372 S5D) we see no significance (Supplementary Figure S5E-G), indicating that these genes are
373 stratifying patients only in the presence of radiation (Figure 4B), consistent with our model's
374 prediction of these targets as potential radio-sensitising agents.
375 Lastly, we investigated whether there was a continuous relationship between the lowest level of
376 a radio-sensitising gene in a patient and their survival following treatment with radiotherapy. This
377 assumes that the level of radio-sensitisation in a patient is rate-limited by each of our model-
378 predicted radio-sensitising agents. For each patient, we calculated the lowest linear copy number
379 of each of the 19 genes (Figure 4C) and then used this continuous variable to predict survival in
380 patients exposed to radiotherapy. The survival area plot for this analysis is shown in Figure 4D,
381 showing significant association between the minimum CNV level of the radio-sensitising genes
382 and survival (Cox proportional hazards regression; HR=2.91, P=0.07). This association does not
383 exist for survival among patients not treated with radiotherapy (HR=1.19, P=0.6), indicating this
384 relationship only exists in the presence of radiation. Collectively, these findings demonstrate that
385 low CNA and low RNA expression of our predicted radio-sensitising genes are significant
386 predictors of improved survival in patients receiving radiotherapy. However, our modelling and
387 statistical analysis of clinical outcomes also shows that many patients are radioresistant and so
388 this necessitates broader choices of therapeutic options.
389

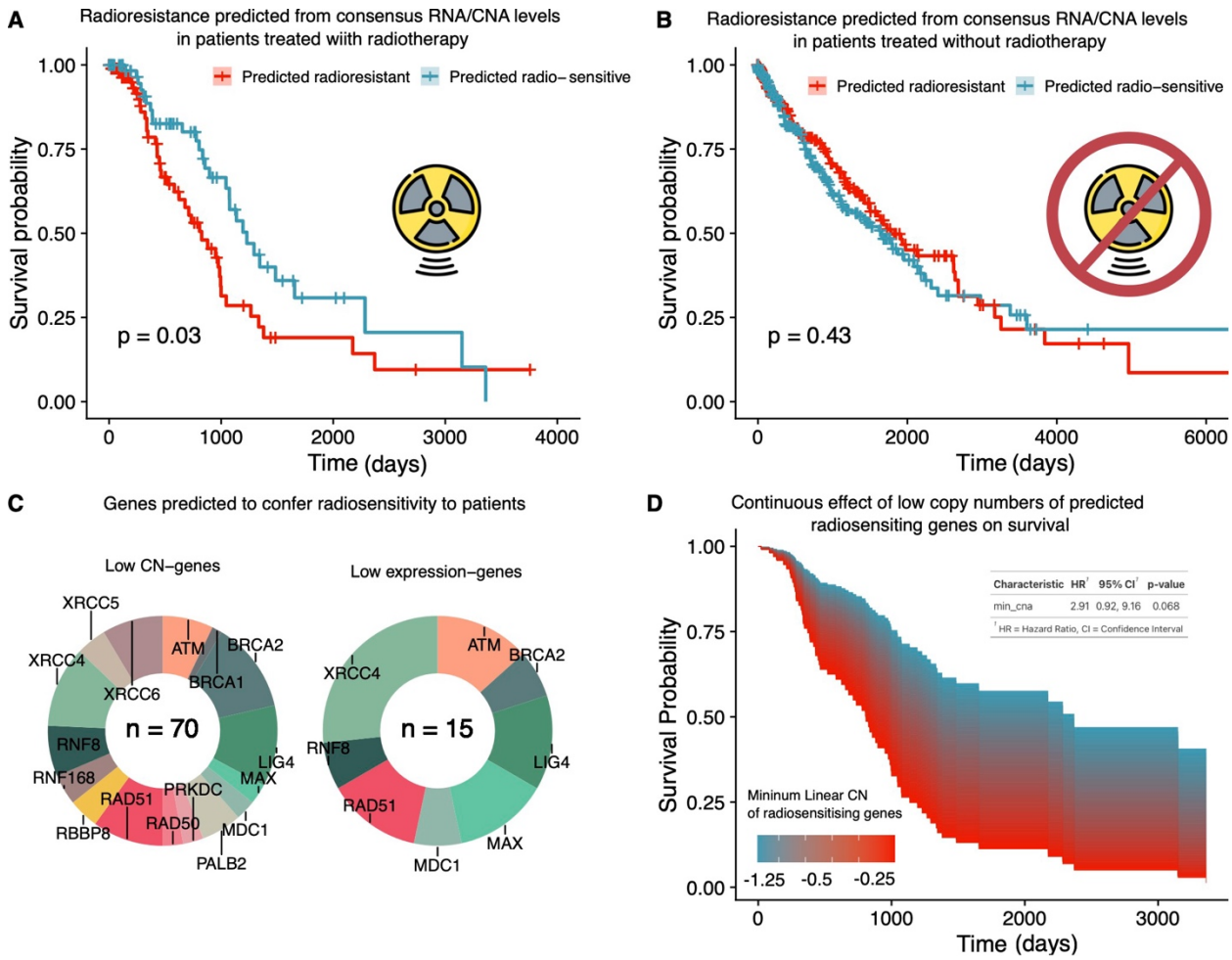


**Figure 4. *In silico* predictions stratify radiation-treated patients into radiosensitive and radioresistant strata. A, B)** Kaplan-Meier survival curves showing the differences in survival between predicted radioresistant patients (red) and radiosensitive patients (blue) for patients treated with radiation (B) and without radiation (C). The x-axis indicates the time (days) since diagnosis and y-axis indicates the survival probability. **C)** Pie-charts showing the genes with the lowest copy number (left) or expression (right) for each patient predicted to be radiosensitive. **D)** Continuously coloured survival area plots showing the effect of the minimum copy number of radio-sensitising genes on survival. The x-axis indicates the time (days) since diagnosis and y-axis indicates the survival probability. Colour indicates the minimum copy number of genes within our predicted set, with blue indicating lower copy number.

## *In silico* screens identify MYC and ATR inhibitor as a cancer-specific treatment combination

To find further treatment combinations that are effective specifically on cancer cells we looked at different combinations of targeted therapies that could increase the difference in death between healthy and cancer cells. Combination treatments are also likely to reduce resistance compared to monotherapy[51,52]. We performed *in silico* screens of pairwise combinations of 95 druggable targets in the model for SW1573, NCIH1792, HCC827, PC9, A549 and NCIH1993 cell lines (see Methods). We isolated the treatment combinations that were predicted to have an additive effect on overall survival (proliferation - death) when compared to the most effective single treatment (see Methods and Supplementary Figure S6). This was measured for survival rather than death because combination therapy seeks to limit oncogenic growth as well as induce

411 apoptosis, as opposed to radiotherapy which has the primary aim of causing apoptosis or DNA-
412 damage associated death[53]. We then clustered these treatments into those that have a similar
413 effect on the cell lines to highlight patterns of response and profiles of sensitivity. This produced
414 24 different subclusters, labelled *I* - *XXIV*, in order of their efficacy vs the most effective single
415 treatment (see Methods). We see that clusters *I, II* and *IV* are the only broad-spectrum
416 treatments that have a wide, additive effect across all cell lines tested (Figure 5).
417 We next compared our simulated results to experimental data generated by Nair and colleagues
418 measuring the additive score of various drug combinations in SW1573, NCIH1792, HCC827, PC9,
419 A549 and NCIH1993 (Supplementary Figure S7)[54]. We see that the data shows significant
420 concordance with our predictions across all cell lines tested. Comparing Higher than Single Agent
421 effect (HSA) to our predictions of additivity, we see moderate, but significant correlation (Kendall
422 Tau = 0.16; p-value = 8.176e-11) across all drug combination predictions. Given the large
423 proportion of intermediate or no additivity predicted by our model and measured by Nair and
424 colleagues, we also looked at correlation of purely additive combinations as predicted by our
425 model (those shown in Figure 2). In these groups we see stronger correlation (Kendall Tau = 0.27;
426 p-value = 1.7e-07,). Correlations of the most additive treatments in Clusters *I* - *V* show stronger
427 correlation still (Kendall Tau = 0.37; p-value = 2.3e-07). For reference, the average Pearson's
428 correlation across experimental replicates in GDSC[55], CTD[56] and PRISM[57] drug screening
429 platforms is ~0.30[58]. We also find that the model's predictions can recapitulate the sensitivities
430 of different cell lines to specific drugs (See Supplementary Figure S8 and Supplementary Notes).
431 These results indicate that our predictions correlate with published data and correlation
432 improves when discriminating between more additive therapies.
433 According to the simulations, the most effective group of drug combinations by average additivity
434 across cell lines are those targeting AKT and MAPK pathways (Cluster I). These have a uniform
435 effect across cancer cell lines, increasing death from the untreated (baseline) level while also
436 causing growth arrest (Figure 5). This combination does not discriminate between oncogenic or
437 healthy cells, so although it is a reliable means of treating a wide range of mutational profiles in
438 cancer, it is also likely cytotoxic to healthy tissue. Cluster II discriminates between healthy cells
439 and tumorigenic cells and is composed of ATR and MYC inhibition. It limits growth to be on par
440 (proliferation = 1) with healthy cells, while increasing death only in cancer cell lines. The
441 remaining highly additive clusters are those dealing with RTKs mutated in specific cancer cell
442 lines. For example, Cluster *III* is additive in cell lines with *EGFR* gain-of-function mutations, while
443 Cluster *V* is additive in NCIH1993, a cell line with a *MET* mutation. These clusters illustrate the
444 importance of cell line-specific key genetic determinants of response that govern the most
445 effective and additive combinations needed for efficacious treatment. However, given drugs
446 within Cluster II are broadly effective regardless of mutational profile, while sparing healthy cells,
447 we decided to explore further the mechanism of action of this line of therapy.
448

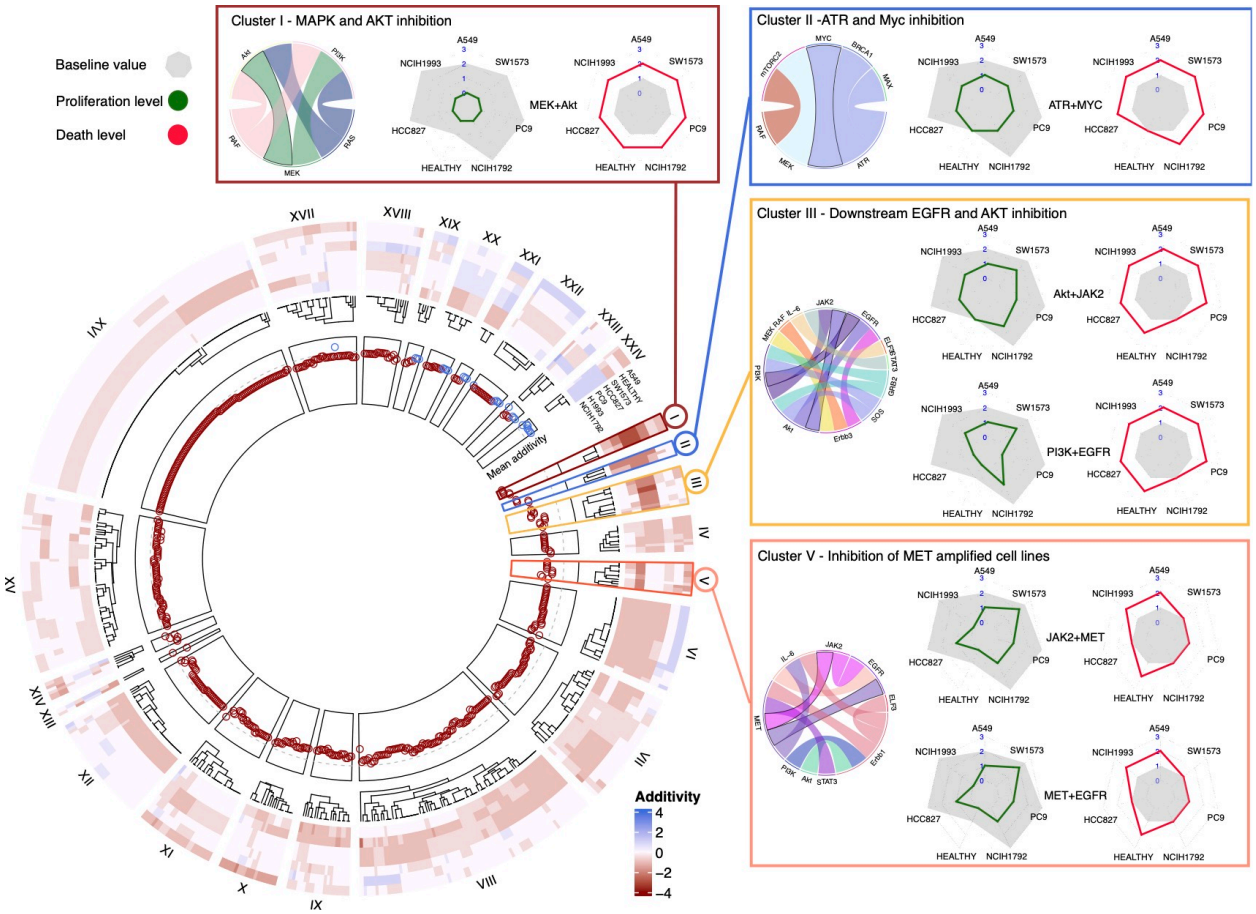


**Figure 5. Systematic *in silico* combination screen on NSCLC adenocarcinoma network model.** Circular heat map showing the additive effect of drug combinations on selected NSCLC adenocarcinoma cell lines. Columns (spokes of the wheel) are the drug combinations and have been clustered into groups (I-XXIV) of drugs that have a similar additive effect. Red indicates those combinations that have a greater additive effect, while blue represents those drugs with antagonistic effects (the drugs cancel one another out). The plot in the inner wheel of the circle shows the mean additive effect of a drug across all cell lines and is red for those drug combinations with overall additive effect and blue for those antagonising one another. Clusters I, II, III and V, and the most effective combinations within, them are highlighted. Circular chord diagrams illustrate the various drug combinations within a cluster and radar plots show the absolute levels of proliferation (green) and death (red) after drug treatment when compared to the baseline (grey). These are shown for specific drug combinations that are outlined in black in the chord diagrams.

## Combined MYC and ATR inhibition is predicted to limit cell growth and kill cancer cells through double stranded breaks

The model predicts that inhibiting MYC limits proliferation and causes cell death when combined with ATR inhibition in cancer cell lines without affecting healthy cells. This is in line with our earlier prediction of the effect of MYC inhibition in combination with radiotherapy. ATR inhibition alone is predicted to have little impact on all cell lines tested, whereas MYC and ATR inhibitions are predicted to increases cell death in cancer cell lines more than in healthy cells (Figure 6A). To assess the effect of these perturbations on the entire model state, we used Principal Component Analysis (PCA) to visualise the entire state space of the model following treatment with ATR and MYC inhibitors (Figure 6B), seeing that the treatment predicts to affect healthy cells (bottom left)

471 less, while leading to a large difference in cancer cell lines (top). The loadings for different model
472 variables are also plotted as vectors to highlight those that contribute to the separation in
473 coordinate space of the PCA and represent variables that are changing mostly after perturbation.
474 We predict that following treatment there is an increase in p15, G2/M arrest and toxic NHEJ,
475 which is responsible for the increase in cell death. The variables and the regulatory interactions
476 that exist between them are plotted in Figure 6C. This suggests how ATR and MYC inhibitions
477 combine to limit oncogenic signalling, as well as the induction of DNA damage-associated death
478 in cell line PC9 (the remaining cell lines in Supplementary Figure S9). MYC inhibition is predicted
479 to disrupt the oncogenic operation of the cell cycle, while also inhibiting apoptosis and
480 homologous recombination. Inhibiting ATR could then increase single-ended double strand
481 breaks (seDSB) by preventing the cell from responding properly to replication stress, which is
482 higher in cancer cells due to their higher rate of proliferation. MYC inhibition prevents proper
483 repair of seDSB owing to the loss of MRN and thus ATM activation, leading to toxic NHEJ[46].
484 Healthy cells are also predicted to be less affected by the inhibition of MYC, which is more highly
485 activated in every cancer cell line (Figure 5C). As a result, inhibition of MYC and ATR is predicted
486 to have the greatest therapeutic window of all the treatments we simulate and could be a
487 promising therapeutic candidate applicable to a wider variety of mutational backgrounds.
488 As of writing, MYC inhibitors are in early stage trials[59–61], however, other specific drug
489 combinations that we predict to be additive are composed of clinically approved drugs. Unlike
490 MYC and ATR inhibition, these treatments are only effective in selective cell lines. To explore this
491 effect more systematically, we investigated the key explanatory mutations in cell lines that drive
492 responses to various groups of targeted therapy combinations that we predicted as being
493 additive.
494

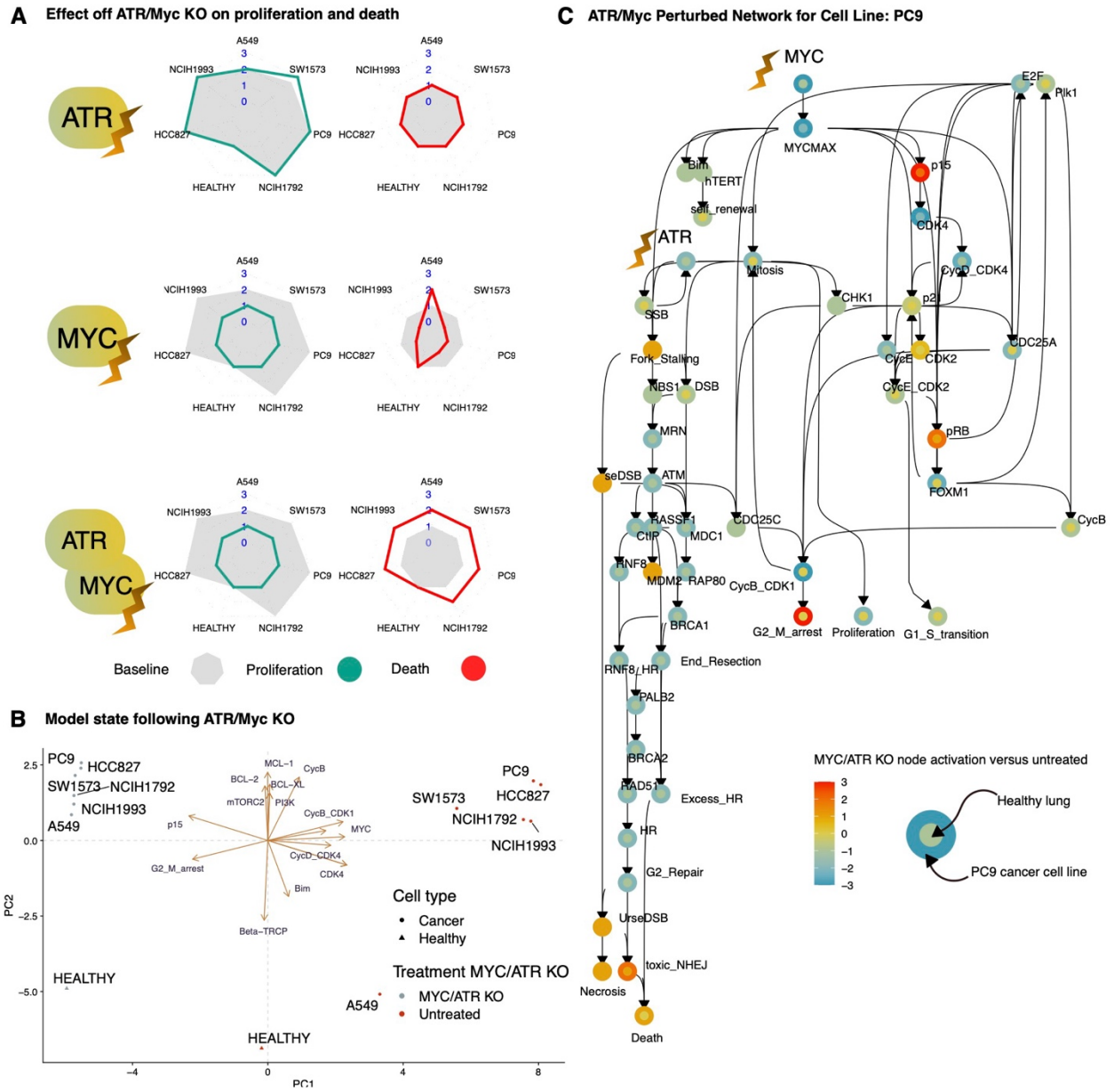


**Figure 6. Mechanistic analysis of combined ATR and MYC inhibition illustrates their induction of DNA damage associated death. A)** Radar plots showing the absolute levels of proliferation (green) and apoptosis (red) after MYC inhibition, ATR inhibition and combined MYC and ATR inhibition. The baseline growth and proliferation are shown in grey. **B)** PCA showing the model states of different cell lines following treatment with MYC/ATR inhibition. Cancer cell lines are plotted as circles and healthy cells (lacking oncogenic mutations) are triangles. Untreated cells are in red and treated cells are in red. Vectors are also included in the PCA to visualise the loadings of different variables and how they contribute to the separation of *in silico* samples in 2D space. **C)** Subnetwork of the model, covering the proteins and variables that changed after treatment of MYC/ATR inhibitors in PC9 (a cancer cell line). Colour of the node illustrates the difference between ATR/MYC inhibition vs untreated (blue for a relative decrease in activation and red for an increase) in PC9 (outer circle) and the difference in healthy lung cells (inner circle).

## EGFR and TP53 mutations explain additive response to combined MAPK and AKT inhibition

Given that treatment effectiveness varied with small changes in mutational profile, we aimed to find which mutations have the greatest explanatory power in drug response, as these could be used as biomarkers. Accordingly, we visualised drug additivity in the most effective combination clusters and aligned this with the mutations used to model the cell lines (Figure 7A). We predict that EGFR is strongly associated with response to treatments in clusters *I, III* and *V*. For example, treatments in cluster *I* (MAPK/Akt inhibition) are most additive in PC9 and HCC827 (EGFR mutant cell lines). Similarly, treatments in Cluster *III* are most additive in cell lines that contain EGFR gain-of-function, while the opposite is true for Cluster *V.* Additionally, TP53 mutations are associated with response to clusters I, and III with the most additive responders to those clusters of combinations being NCIH1993, HCC827 and PC9 (Figure 7A).

We used a linear model to quantify the relationship between cell line mutations and their responses to combination treatments and find the most explanatory mutations for additive drug combinations responses in the different cell lines (See Methods). We found that TP53 and EGFR mutations are most broadly associated with an additive response to the tested combinations (Figure 3B). However, for Cluster V we see a negative coefficient for EGFR mutations, indicating that the absence of this mutation is required for additivity to be observed. Instead, a MET amplification (as is the case for NCIH1993) is associated with additivity in this cluster (Figure 7B). These results suggest which mutations determine response in different mutational profiles, and highlight EGFR, TP53 and MET as key for patient stratification. Such insight is key to bridging therapeutic responses and oncogenic mutations, allowing us to stratify patients to find the most suitable course of treatment for a given situation.

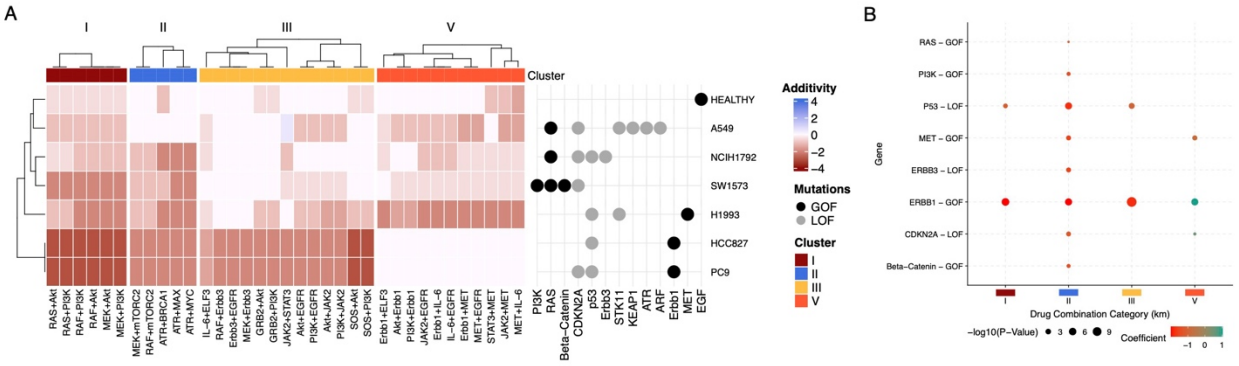


**Figure 7. EGFR and TP53 mutations explain the response of cell lines to targeted combination therapy. A)** Heatmap illustrating aligning the mutations of cell lines (right) with their response to the most effective drug combination clusters from Figure 5 (I in red, II in blue, III in yellow and V in orange). Columns of the heatmap indicate specific drug treatments and rows indicate cell lines. The colour in the heatmap refers to additivity with red indicating strongly additive behaviour and white indicating no additivity. The schematic (right) shows mutations as columns and cell lines as rows, with gain-of-function mutations for a cell line and loss-of-function (grey). **B)** Plot showing the coefficients of the linear model relating mutations present in a cell line (y-axis) to additive response against drug clusters (x-axis). Colour represents the value of the coefficient, such that blue indicates a mutation is associated with additive response to a cluster and red indicates that a mutation's absence is associated with additive response to a cluster. Size of the dot represents the significance of the association.

## Discussion

Matching the variety of mutational profiles exhibited by NSCLC adenocarcinoma with the wide range of existing and potential therapeutic options presents a huge combinatorial challenge. Here, we showcase an *in silico* platform for executable modelling to explore this immense therapeutic landscape. By using the broad and extensive prior knowledge from published experimental research, we constructed an executable model that can explore treatment options in an efficient and mechanistically interpretable fashion. Using this platform, we assessed ~66,000 predicted combinations of targeted therapy and radiotherapy, finding the most suitable and effective treatment options, specific to given genotypes. We also investigated how mutations combine and determine response to therapy, and the mechanisms that underpin this, allowing for testable hypotheses to expand our understanding of oncogenic signalling, and demonstrate a novel method for stratification of patient sensitivity to radiotherapy using clinical data based on targets identified by the *in silico* model.

Finding that healthy cells are more sensitive to single-agent treatment than cancer cells in our *in silico* modelling and motivated by the need for combination treatments to prevent resistance[51] we explored combinations of drugs with one another and with radiotherapy. We find that the most effective cluster of drug combinations (Cluster *I*) consists of combined MAPK/PI3K inhibition. AKT and MAPK are downstream processors of all growth pathways in the *in silico* model and most oncogene mutations found in lung cancer target members of these pathways or upstream regulators (e.g., KRAS, PIK3CA, EGFR, MET, ALK). MAPK/AKT inhibitors are often used as positive controls for synergy experiments and have previously been flagged as highly additive in lung cancer[54,62]. However, healthy cells also rely on these pathways and so their inhibition can cause side-effects[63]. We were able to identify other combinations that specifically targeted cancer cells owing to mutations in the NSCLC adenocarcinoma cell lines. Specifically, we found that EGFR is an important determinant for the additive response to several potential combinations. We also find that absence of EGFR mutation is as an important determinant of response to MET inhibitor combinations than the presence of a MET mutation itself. In general, we show that the mutational status of receptors is important in determining additivity to targeted therapy, and so a patient's mutational status of EGFR, MET among others are particularly informative in determining personalised therapeutic options.

Most combinations have a similar effect on healthy and cancer cells. However, for both radiotherapy and combinations of targeted therapy, we predict that MYC has strong potential in targeting cancer cells without affecting healthy cells. MYC is frequently overexpressed in cancer, owing to its central position in the hourglass topology of pathways governing regulation and effect[64]. This importance makes resistance to MYC-targeting drugs extremely difficult[65]. This structure is reflected in our model and means that for the heterogeneity of cancer mutational profiles, they broadly produce a higher activation of MYC and its downstream targets[65]. This puts MYC in a unique place as a promising therapeutic target with inhibition well tolerated in healthy tissue[66]. However, despite advances in developing inhibitors targeting MYC[67,68], none are currently clinically approved for treatment. Our work underlines the exciting prospect of MYC as a therapeutic target and goes further in suggesting ATR as a parallel target, offering the option to further exploit weaknesses in cancer cells DNA damage repair. We show that by targeting cancer cell reliance on MYC overexpression and the dependence of DSB

586 repair on MYC via the MRN complex, one can produce therapeutics that are robust and broadly
587 effective against varied mutational profiles. However, this depends on how sensitive DDR
588 pathways are to MYC inhibition as MYC inhibitors such as Peptomyc[61] and OMO-103[69] are likely
589 to be less effective compared to the full knockout simulated by the *in silico* model. Our model
590 suggests that the effect of MYC inhibition on cancer cells is due, in part, to its regulation of DSB
591 repair via the MRN complex. Prior work in cell lines found that DDR was robust to MYC
592 downregulation[70]. Our analysis shows that a clinical signature (derived from *in silico* simulations)
593 including MYC and its binding partner MAX act as a predictor of radiosensitivity (Figure 4A).
594 Together these results suggest that the link between MYC and radio-resistance should be
595 investigated further.
596 Radiotherapy remains a main component of the standard of care for NSCLC adenocarcinoma
597 treatment[1]. A key factor in response to radiotherapy is TP53, with mutations disabling its
598 activation, either in the TP53 gene or upstream, frequently seen across all tissues and often
599 associated with therapy resistance[71,72]. The exact effect on radio-sensitisation is contentious,
600 with TP53 loss-of-function often leading to radio-resistance[73,74], but contributing both to radio-
601 sensitivity and radio-resistance in different contexts and tissues[75–77]. We predict that TP53 loss-
602 of-function mutations in NSCLC adenocarcinoma are broadly radio-protective, yet in the
603 presence of specific mutational profiles can be radio-sensitising. A subset of potential treatments
604 is radio-sensitising despite TP53 mutation, and some are completely invariant to it (Figure 3B).
605 This suggests that radio-resistance can be overcome, or pre-empted, by identifying the correct
606 treatment and offers hope that this may hold with a broader range of resistance mechanisms.
607 Due to the increased toxicity of radio-sensitising treatments, we predict it will be important to
608 stratify patients by TP53 mutation[78] for drug-radiotherapy treatments. TP53 mutation occurs
609 early in NSCLC adenocarcinoma[79] and is strongly associated with metastatic seeding sub-clones.
610 As metastases are the key driver of patient death[80], treatments that target clones that are
611 mutated in drivers of metastases are especially important. Our identification of radio-sensitising
612 treatments that overcome TP53-driven radio-resistance satisfies a key part of this. We further
613 use our model to identify a 19-gene signature that, by combining CNV and RNA-expression data,
614 stratifies patients into radiosensitive and radioresistant groups. We suggest this can be used to
615 better target radiotherapy treatment to those patients that are most likely to benefit from it in
616 the clinic.
617 Radio-sensitising combination treatments are already being explored on a small scale, for
618 example as part of the CONCORDE clinical trial[81], and we demonstrate the potential of this
619 approach with our large scale *in silico* and *in vitro* screens. We validate our *in silico* model
620 predictions in a focussed CRISPR screen and find that the model prediction of DNA-damage
621 related cell death is a good indicator of sensitisation. We were unable to test our predictions in
622 cases where gene knock-out was lethal to cells without radiation, e.g., in the case of MYC. Such
623 knock-outs are less well tolerated than intervention with drugs, as demonstrated by MYC
624 inhibitors such as Peptomyc[61] and OMO-103[69] being well tolerated in clinical trials, and so further
625 studies with inhibitors may prove fruitful. Calibrating contributions for targeted treatments and
626 IR on different mechanisms of cell death (i.e., apoptosis vs DNA-damage associated cell death) is
627 challenging. Indeed, we find that our model is more accurate when we output DNA-damage
628 associated cell death and apoptosis separately. It is of especial note that inhibition of 53BP1 leads
629 to radio-sensitisation in cancer cell lines but not in healthy cells. 53BP1 loss is a common

630 resistance mutation to PARP inhibitors[16], and thus this may suggest a collateral sensitivity that
631 can be exploited for second line treatments. 53BP1 loss is a common resistance mutation to PARP
632 inhibitors[16], and thus this may suggest a collateral sensitivity that can be exploited for second line
633 treatments.
634 Current experimental approaches to identify combinations of therapies involve performing
635 global screens of perturbations on various cell models of NSCLC adenocarcinoma with differing
636 mutational profiles. This can be done with drugs or CRISPR knockouts alongside 'omics
637 measurements, observing the survival of the treated cells to understand hidden mixtures of
638 lethal targets[54,62,82]. For example, Jaaks *et al.* tested 2025 pairwise drug combinations *in vitro*
639 using the Genomics of Drug Sensitivity in Cancer (GDSC) cell line screening platform to identify
640 biomarkers of response to combination therapies[55,83]. While such screening strategies can yield
641 extremely high throughput, identifying target hits and biomarkers of their response across a
642 broad range of unrelated backgrounds, there are practical drawbacks of such approaches. For
643 example, developing a mechanistic understanding is hampered by off-target effects in drugs and
644 CRISPR guide RNAs[84], which can lead to false positive[85] and false negative results[86]. Additionally,
645 these screens are time-consuming and expensive and cannot be performed on rarer genetic
646 profiles easily, leading to results biased towards the most common cellular models.
647 Computational methods can circumvent some of these technical issues and provide
648 complementary screening approaches. For example, Eduati *et al.* use perturbation screening data
649 to train a network to uncover patient-specific mechanisms underpinning pancreatic cancer[87].
650 Their model was trained using perturbation screens of patient biopsies and tested pairwise
651 combinations of 12 targetable nodes in the network. In our work, we build on this by using more
652 coarse-grained, but large-scale modelling of biological processes, allowing for more targetable
653 nodes (i.e., 95 druggable targets), and integrated radiotherapy. Our modelling approach also only
654 require mutational data for individualisation of our generic model, rather than training on
655 combinatorial perturbation screening on cancer biopsies, which are more expensive and invasive
656 and have limited clinical applicability. Fröhlich *et al.* used a larger, pan-cancer mathematical
657 model to predict effective drug combinations[88]. However, the complexity of the parameter space
658 of these models makes them computationally intensive to run on novel mutational backgrounds
659 and mathematical models with many parameters more prone to overfitting than coarse-grained
660 executable biological models. Others have used phospho-proteomic changes[62] and machine
661 learning[89] to predict drug sensitivity. However, while the accuracy of the method was high[62], it is
662 not clinically feasible currently to take phosphoprotein measurements of patients to determine
663 drug response. Moreover, machine learning based approaches used to predict synthetic lethal
664 targets lack the mechanistic interpretability of this method and often neglect radio-therapeutic
665 combinations due to the relative lack of genome-wide data on radiotherapy sensitising agents.
666 Our *in silico* model incorporates radio-resistance which is important to consider as it is already a
667 common clinically used therapy.
668 In this study we demonstrate how executable modelling enables system-level experiments to be
669 rapidly conducted. In addition, our *in silico* approach allows mechanistic transparency, providing
670 insight into why treatments do and do not work and the biological underpinnings of mutational
671 profile-specific sensitivities. Using mutational data, our executable models can be individualised,
672 paving the way for 'digital twins' of tumours for testing hundreds of thousands of therapeutic
673 options. We envisage that executable models have the potential to improve personalised therapy

674 in NSCLC adenocarcinoma patients and help predict and combat the development of resistance
675 to treatment.
676
677
678 ## Methods
679 We performed all visualisation and data analysis using the programming language R, and data
680 visualisation packages ggplot2, ComplexHeatmaps and Circularize. Figure 1A was created with
681 BioRender.com.

682 **Qualitative networks**

683 We represent the NSCLC adenocarcinoma signalling network as a discrete qualitative network[22].
684 This represents each gene, protein, or process as a node with multiple finite values of the range
685 (0-3), where 0 represents very low activity e.g., due to a loss-of-function mutation, 1 represents
686 normal behaviour, 2 elevated activity and 3 represents very high activity e.g due to a gain-of-
687 function mutation. This was built, tested, and analysed using the open source webtool,
688 BioModelAnalyzer (BMA, https://biomodelanalyzer.org) and associated command line tools
689 (https://github.com/hallba/BioModelAnalyzer). The model and code for analysis is available at .
690 Nodes in the network represent biological factors such as proteins or subunits of proteins. Input
691 nodes represent growth factors, or in some cases amplification as with ATM. Output nodes are
692 representing phenotypes such as death and proliferation. Regulatory interactions (both
693 activating (→) and inhibitory (⊣)) are represented by edges between nodes. The level of activity
694 of a node responds to the upstream levels of regulators of that node. This is determined by a
695 mathematical function, unique to each node that integrates the levels of the upstream regulators
696 to determine the target level of the target node at the next time-step, with the activity of each
697 node changing by at most 1 unit per time step. This function is termed the target function. The
698 default target function is the average of the activating upstream regulators, negated by the
699 average of the inhibiting regulators (*avg(pos)-avg(neg)*). More complex functions are used as
700 needed to recapitulate specific experimental behaviours (see below). These target functions
701 along with corresponding references are described in Supplementary Table S2. A summary of the
702 nodes included, and their HUGO gene symbol are summarised in Supplementary Table S3.
703 For a specified starting state of all nodes, the model will update node values synchronously, such
704 that there will be one deterministic stable attractor of the network. This attractor can be a fixed-
705 point attractor with one end state, or it can be a loop of states that the model cycles through,
706 called a cyclic attractor. We test the model from all possible initial states, which allows for
707 multiple attractors to be reachable, termed a bifurcation. In the case of a loop or bifurcation, the
708 upper and lower bounds across all attractors are returned. This is done using the algorithm
709 described in Cook *et al.*[90]. The algorithm for network simulation is found in Schaub *et al.*[22]. If
710 there is no single attractor, we use the midpoint of the upper and lower bound as an
711 approximation of the overall level of the node.

712 **Model construction and testing**

713 Experimental evidence for each model edge is described in Supplementary Table S1. We manually
714 curated a separate set of 26 papers describing the behaviour of different NSCLC adenocarcinoma

715 cell lines under various perturbations and conditions. From these papers 69 separate
716 experimental conditions were modelled and used to optimise the target functions of the model.
717 This is described in Supplementary Table S2. Accuracy was calculated by taking the number of
718 experiments recapitulated, versus the total number of experiments. An experiment was
719 considered recapitulated if the predicted direction of change of the model is the same as that of
720 the experiment.

721 **Mutational profiles for all cell lines were drawn from Cell Model Passports**

722 To model cell lines we used mutational data from Van der Meer *et al.* as of 04/01/2023[25].
723 Mutations were modelled if they were listed as a driver or a deletion for a node in the model. If
724 annotated as a gain of function the respective node was set to the maximum value, if a loss of
725 function or a deletion the node was set to zero, except in the case of ATM. After the results of
726 the first CRISPR screen, we observed that ATM knock-out was still effective in NCIH1373 and
727 NCIH23 cells despite an ATM mutation observed in both, therefore we model this as a deficiency
728 but not complete homozygous knockout of ATM. We focussed on annotated driver genes and
729 complete deletions so as not to over-specify the model, and to focus on those changes that were
730 likely to be consistent within the population of cell lines[91].

731 **Mutational profiling of cell lines used in radiotherapy CRISPR screens**

732 Mutational data was derived using publicly available datasets, principally DepMap and
733 corroborated using western blotting (*e.g.*, TP53 status). Radiation sensitivity was assessed using
734 colony forming assay, and longer-term cell viability assays (e.g., cell-titre glo >7day timepoint)
735 and assessed against published literature.

736 **Modelling of combination and monotherapy**

737 To find effective treatments, we inactivate (set target function to a minimum) or activate (set
738 target function to maximum) all nodes representing druggable nodes in the network either singly
739 or in a pair-wise combination, using the BMA Command Line tool BioCheckConsole. For each
740 node in the network, we curated a list of drugs that could target nodes within the network,
741 finding 95 candidate drugs using the druggable proteome in The Human Protein Atlas
742 (https://www.proteinatlas.org/humanproteome/tissue/druggable; Accessed 04/08/2023). We
743 evaluate these perturbations by identifying the stable state of the network for death and
744 proliferation as outlined in the 'Qualitative Networks' section above. To have a single value to
745 predict cell growth we take the difference between Proliferation and Death.
746 For combination therapy we simulated these drugs together and studied their interaction using
747 a value we describe as additivity. This is analogous to the experimentally determined Higher than
748 Single Agent effect (HSA) and describes the growth of cells after combined drug treatment
749 relative to the most effective (minimum viability) of the individual drugs in the combination.
750 Combination treatments were clustered using the k-means algorithm to find groups of therapies
751 with similar levels of additivity across cell lines.

752 **Modelling of radiotherapy**

753 To model the effects of radiotherapy, we increase the `Radiotherapy` node to maximum. This
754 leads to increases in the single and double strand break nodes. To model the ability of the cell to
755 repair these insults, we allow these nodes to activate repair mechanisms, while also activating
756 `UrDSB` (Unrepaired DSB). If the repair mechanisms are active, as in healthy cells, this means that
757 UrDSB is inhibited by the activity of those mechanisms to represent the initial insult due to
758 radiotherapy being resolved without causing death, while any damage to the repair pathways
759 will let DSB activate UrDSB and in turn leads to death. Unrepaired SSB are modelled as leading to
760 single-ended or blunt ended DSB (seDSB and DSB) respectively but not leading to death by
761 themselves.
762 We model radio-sensitisation as the increase in death, decrease in proliferation, or decrease in
763 overall survival (proliferation - death) in the combination vs the most effective of the two possible
764 monotherapies (knock-out alone or IR alone).

765 **CRISPR knockout of radioprotective and radio-sensitising genes**

766 A CRISPR screen was performed using a pooled library across the 6 NSCLC, Cas9-expressing, lines
767 using 1Gy given twice over 24 hours (i.e., 2Gy in 2 doses over 2 days). Cells were irradiated using
768 an IBL 637 Irradiator (CS 137 gamma rays below sample). Cells were harvested from day 7 to day
769 31 (up until cells reached 10-12 doublings) and DNA was prepared for next generation
770 sequencing. Hits were identified using MAGeCK RRA (version 0.5.8). Cut-offs of FDR<0.2 and
771 FDR<0.1 were used to define significant depleted genes.
772 Due to the *in vitro* CRISPR screen considering all 20,000 human genes, when a knock-out was
773 observed to have an effect in only a subset of the cell lines it was not possible to conclude
774 whether this was due to a vulnerability contingent on a specific mutational profile, or the power
775 of the screen. For this reason, we measure and compare the number of cell lines in which a knock-
776 out was radio-sensitising in the CRISPR experiments vs the *in silico* model (i.e., recurrence).
777 A second screen was conducted with a focussed panel, across the SW1573, SW1573 *TP53*$^{-/-}$, A549
778 and A549 *TP53*$^{-/-}$ cell lines and AZSA-011N organoids. After 72 hours, we irradiated cell cultures
779 with a single fraction of 4Gy. Post-irradiation, precisely after 1 hour, 24 hours, and 48 hours,
780 irradiated and non-irradiated plates were fixed for immunofluorescence.
781

782 **Generation of organoids normal tissue organoids**

783 Patient derived lung organoids (PDO) were isolated from adjacent normal tissues from consented
784 NSCLC patients at Royal Papworth Hospital via the Royal Papworth Hospital Tissue Bank
785 application ID T02612 / East of England - Cambridge East Research Ethics Committee reference
786 18/EE/0269.
787

788 **Cell culture**

789 HCC-44-Cas9, SW1573-Cas9, H1792-Cas9, H1373-Cas9, H358-Cas9 and H23-Cas9 cell lines were
790 maintained in RPMI 1640 (Gibco) supplemented with 10% FBS (Biowest), 1% GlutaMax (Gibco)
791 and 1% pen/strep (Gibco). Cell lines were passaged every 3/4 days by dissociating to single cell
792 using Accutase (Biowest).

793 **Genomic DNA isolation and Next Generation Sequencing (NGS)**
794 Genomic DNA (gDNA) was isolated using the QIAamp DNA Blood Midi or Maxi Kit (Qiagen)
795 according to manufacturer's instruction. NGS libraries were prepared in a two-step process: the
796 integrated lentiviral cassette containing the gRNA was amplified from gDNA. Forward primer 5'
797 ACACTCTTTCCCTACACGACGCTCTTCCGATCTCTTGTGGAAAGGACGAAACA 3' with reverse primer
798 5'TGACTGGAGTTCAGACGTGTGCTCTTCCGATCTACCCAGACTGCTCATCGTC 3' was used for this.
799 PCR reactions with 5µg gDNA per well were set up using the Q5 Hot Start High-Fidelity 2× Master
800 Mix (NEB #M0494) in a total volume of 50µl. PCR reactions were scaled accordingly to amplify
801 the gRNAs at a coverage of at least 200-fold. The PCR products were then purified using QIAquick
802 PCR Purification Kit (Qiagen #28106). Final NGS libraries were generated using 2.5ng of the
803 purified 1st PCR product using the dual-indexing Illumina-compatible DNA HT Dual Index kit
804 (Takara #R400661). 2nd PCR products were purified with AMPure XP beads (Beckman Coulter
805 #A63881) at an 0.7 ratio. Purified 2nd step libraries were quantified using the Qubit dsDNA
806 Quantification Assay Kit (ThermoFisher) and sequenced on NovaSeq6000 by PE50bp with a 30%
807 PhiX spike-in.
808
809 **Genetic modification of p53 status of NSCLC cell lines**
810
811 The SW1573 line underwent TP53 knockout using a standard CRISPR-based knockout approach
812 to generate a polyclonal TP53 knockout population. Loss of TP53 was confirmed using PCR and
813 western blotting.
814

815 **Stratification of patient data using results from model**
816 Clinical and genomic data for lung adenocarcinoma (LUAD) and lung squamous cell carcinoma
817 (LUSC) were obtained from The Cancer Genome Atlas (TCGA) Research Network
818 (https://www.cancer.gov/tcga) and the cBioPortal platform[92,93] via the RTCGA.clinical R package.
819 Clinical data was categorized based on whether patients received radiotherapy or not, using the
820 patients not receiving radiotherapy as a positive control. Molecular data included RNA
821 expression and Capped relative linear copy-number (CN) values for each gene (from Affymetrix
822 SNP6) and was extracted via the TCGAretriever R package. To identify patients with low
823 expression or alterations in the genes of interest, the CNA and RNA datasets were combined for
824 both LUAD and LUSC. We identified patients as radiosensitive if they had gene expression or CN
825 values below specific quantile thresholds (5th percentile for CNA, 10th percentile for RNA) for at
826 least one gene in our model-defined set of radio-sensitising genes. To associate patient strata
827 with clinical outcomes we used the Cox proportional hazards regression model in R. To visualise
828 the survival probability over time as a function of the lowest CN we used the R package
829 contsurvplot[94].

830 **Statistical analysis of combination drug sensitivity**

831 For drug combination we use the dataset available from Nair *et al.* (2022) and take all the drug
832 inhibitors they used and compare them to our predictions. Nair *et al.* use HSA and so we
833 compared our value for additivity (see above). For statistical analysis, we visualise t test between
834 HSAs of different treatments for different values of additivity that the model predicts (-3 through
835 1) and compare this to treatments predicted to be not additive. Also, to factor in the ordinal
836 nature of the model's prediction, we calculate overall correlation using Kendall's tau test and bin
837 experimentally measured HSA into 4 quartiles.

838 **Linear regression to identify genetic determinants of response**

839 We separate the drug treatments into the clusters outlined above and train a linear model to
840 relate drug response (measured by additivity) with the mutational profile of the cell lines. P
841 values were adjusted for multiple hypothesis correction between each drug cluster using the
842 method devised by Benjamini & Hochberg (1995)[95].
843

844 ## Acknowledgments

845 This work was supported by Cancer Research UK grant C17918/A28870 (G.J.H. and J.F.), CRUK
846 Convergence Science Centre, Experimental Cancer Medicine Centre and NIHR Biomedical
847 Research Centre (L.P., U.B. and J.C.), and National Institute for Health Research University College
848 London Hospitals Biomedical Research Centre (J.F.).
849
850

851 **References**


852 1. Guo, H. *et al.* "How Long Have I Got?" in Stage IV NSCLC Patients With at Least 3 Months Up to
853 10 Years Survival, Accuracy of Long-, Intermediate-, and Short-Term Survival Prediction Is Not Good
854 Enough to Answer This Question. *Front. Oncol.* **11**, (2021).
855 2. Li, J. & Kwok, H. F. Current Strategies for Treating NSCLC: From Biological Mechanisms to Clinical
856 Treatment. *Cancers* **12**, 1587 (2020).
857 3. Quaresma, M., Coleman, M. P. & Rachet, B. 40-year trends in an index of survival for all cancers
858 combined and survival adjusted for age and sex for each cancer in England and Wales, 1971-2011: a
859 population-based study. *Lancet Lond. Engl.* **385**, 1206–1218 (2015).
860 4. Wu, F. *et al.* Single-cell profiling of tumor heterogeneity and the microenvironment in advanced non-
861 small cell lung cancer. *Nat. Commun.* **12**, 2540 (2021).
862 5. Mok, T. S. *et al.* Gefitinib or carboplatin-paclitaxel in pulmonary adenocarcinoma. *N. Engl. J. Med.* **361**,
863 947–957 (2009).
864 6. Rosell, R. *et al.* Erlotinib versus standard chemotherapy as first-line treatment for European patients
865 with advanced EGFR mutation-positive non-small-cell lung cancer (EURTAC): a multicentre, open-
866 label, randomised phase 3 trial. *Lancet Oncol.* **13**, 239–246 (2012).
867 7. Maemondo, M. *et al.* Gefitinib or chemotherapy for non-small-cell lung cancer with mutated EGFR.
868 *N. Engl. J. Med.* **362**, 2380–2388 (2010).
869 8. Mascaux, C., Tomasini, P., Greillier, L. & Barlesi, F. Personalised medicine for nonsmall cell lung cancer.
870 *Eur. Respir. Rev.* **26**, (2017).
871 9. Overview | Lung cancer: diagnosis and management | Guidance | NICE.
872 https://www.nice.org.uk/guidance/ng122 (2019).
873 10. Zhao, L. *et al.* The Determinant of DNA Repair Pathway Choices in Ionising Radiation-Induced DNA
874 Double-Strand Breaks. *BioMed Res. Int.* **2020**, 4834965 (2020).
875 11. Roos, W. P. & Kaina, B. DNA damage-induced cell death by apoptosis. *Trends Mol. Med.* **12**, 440–450
876 (2006).
877 12. Stokes, W. A. *et al.* Post-Treatment Mortality After Surgery and Stereotactic Body Radiotherapy for
878 Early-Stage Non–Small-Cell Lung Cancer. *J. Clin. Oncol.* **36**, 642–651 (2018).
879 13. Chi, A., Fang, W., Sun, Y. & Wen, S. Comparison of Long-term Survival of Patients With Early-Stage
880 Non-Small Cell Lung Cancer After Surgery vs Stereotactic Body Radiotherapy. *JAMA Netw. Open* **2**,
881 e1915724 (2019).
882 14. Aravindan, N. *et al.* Acquired tumor cell radiation resistance at the treatment site is mediated through
883 radiation-orchestrated intercellular communication. *Int. J. Radiat. Oncol. Biol. Phys.* **88**, 677–685
884 (2014).
885 15. Chuang, R. *et al.* Drug Target Optimization in Chronic Myeloid Leukemia Using Innovative
886 Computational Platform. *Sci. Rep.* **5**, 8190 (2015).
887 16. Clarke, M. A., Woodhouse, S., Piterman, N., Hall, B. A. & Fisher, J. Using State Space Exploration to
888 Determine How Gene Regulatory Networks Constrain Mutation Order in Cancer Evolution. in
889 *Automated Reasoning for Systems Biology and Medicine* (eds. Liò, P. & Zuliani, P.) 133–153 (Springer
890 International Publishing, Cham, 2019). doi:10.1007/978-3-030-17297-8_5.

891 17. Clarke, M. A. & Fisher, J. Executable cancer models: successes and challenges. *Nat. Rev. Cancer* **20**,
892 343–354 (2020).
893 18. Howell, R. *et al.* Localized immune surveillance of primary melanoma in the skin deciphered through
894 executable modeling. *Sci. Adv.* **9**, eadd1992 (2023).
895 19. Kreuzaler, P. *et al.* Heterogeneity of Myc expression in breast cancer exposes pharmacological
896 vulnerabilities revealed through executable mechanistic modeling. *Proc. Natl. Acad. Sci.* **116**, 22399–
897 22408 (2019).
898 20. Silverbush, D. *et al.* Cell-Specific Computational Modeling of the PIM Pathway in Acute Myeloid
899 Leukemia. *Cancer Res.* **77**, 827–838 (2017).
900 21. Talarmain, L. *et al.* HOXA9 has the hallmarks of a biological switch with implications in blood cancers.
901 *Nat. Commun.* **13**, 5829 (2022).
902 22. Schaub, M. A., Henzinger, T. A. & Fisher, J. Qualitative networks: a symbolic approach to analyze
903 biological signaling networks. *BMC Syst. Biol.* **1**, 4 (2007).
904 23. Fisher, J. & Henzinger, T. A. Executable cell biology. *Nat. Biotechnol.* **25**, 1239–1249 (2007).
905 24. Chevallier, M., Borgeaud, M., Addeo, A. & Friedlaender, A. Oncogenic driver mutations in non-small
906 cell lung cancer: Past, present and future. *World J. Clin. Oncol.* **12**, 217–237 (2021).
907 25. van der Meer, D. *et al.* Cell Model Passports-a hub for clinical, genetic and functional datasets of
908 preclinical cancer models. *Nucleic Acids Res.* **47**, D923–D929 (2019).
909 26. Gao, J. *et al.* A novel epidermal growth factor receptor inhibitor for treating lung cancer. *Tumour Biol.*
910 *J. Int. Soc. Oncodevelopmental Biol. Med.* **39**, 1010428317698358 (2017).
911 27. Li, J. *et al.* Inhibition of non-small cell lung cancer (NSCLC) growth by a novel small molecular inhibitor
912 of EGFR. *Oncotarget* **6**, 6749–6761 (2015).
913 28. Chiba, M. *et al.* MEK inhibitors against MET-amplified non-small cell lung cancer. *Int. J. Oncol.* **49**,
914 2236–2244 (2016).
915 29. Fok, J. H. L. *et al.* AZD7648 is a potent and selective DNA-PK inhibitor that enhances radiation,
916 chemotherapy and olaparib activity. *Nat. Commun.* **10**, 5065 (2019).
917 30. Yang, L. *et al.* Inhibition of DNA-PK activity sensitizes A549 cells to X-ray irradiation by inducing the
918 ATM-dependent DNA damage response. *Mol. Med. Rep.* **17**, 7545–7552 (2018).
919 31. Minjgee, M., Toulany, M., Kehlbach, R., Giehl, K. & Rodemann, H. P. K-RAS(V12) induces autocrine
920 production of EGFR ligands and mediates radioresistance through EGFR-dependent Akt signaling and
921 activation of DNA-PKcs. *Int. J. Radiat. Oncol. Biol. Phys.* **81**, 1506–1514 (2011).
922 32. Sato, M., Shay, J. W. & Minna, J. D. Immortalized normal human lung epithelial cell models for
923 studying lung cancer biology. *Respir. Investig.* **58**, 344–354 (2020).
924 33. Wang, M. *et al.* Radiation Resistance in KRAS-Mutated Lung Cancer Is Enabled by Stem-like Properties
925 Mediated by an Osteopontin-EGFR Pathway. *Cancer Res.* **77**, 2018–2028 (2017).
926 34. Singhal, A., Li, B. T. & O'Reilly, E. M. Targeting KRAS in cancer. *Nat. Med.* **30**, 969–983 (2024).
927 35. Xu, T. *et al.* MUC1 downregulation inhibits non-small cell lung cancer progression in human cell lines.
928 *Exp. Ther. Med.* **14**, 4443–4447 (2017).
929 36. Homma, S. *et al.* Nrf2 enhances cell proliferation and resistance to anticancer drugs in human lung
930 cancer. *Clin. Cancer Res. Off. J. Am. Assoc. Cancer Res.* **15**, 3423–3432 (2009).
931 37. Wang, X.-J. *et al.* Nrf2 enhances resistance of cancer cells to chemotherapeutic drugs, the dark side
932 of Nrf2. *Carcinogenesis* **29**, 1235–1243 (2008).

933 38. Xu, Y., Jin, J., Xu, J., Shao, Y. W. & Fan, Y. JAK2 variations and functions in lung adenocarcinoma.
934 *Tumour Biol. J. Int. Soc. Oncodevelopmental Biol. Med.* **39**, 1010428317711140 (2017).
935 39. Cortez, M. A. *et al.* In Vivo Delivery of miR-34a Sensitizes Lung Tumors to Radiation Through RAD51
936 Regulation. *Mol. Ther. Nucleic Acids* **4**, e270 (2015).
937 40. Di Francesco, A. *et al.* The DNA-damage response to γ-radiation is affected by miR-27a in A549 cells.
938 *Int. J. Mol. Sci.* **14**, 17881–17896 (2013).
939 41. Zhou, H. *et al.* RNAi silencing targeting RNF8 enhances radiosensitivity of a non-small cell lung cancer
940 cell line A549. *Int. J. Radiat. Biol.* **89**, 708–715 (2013).
941 42. Wael, H. *et al.* Notch1 signaling controls cell proliferation, apoptosis and differentiation in lung
942 carcinoma. *Lung Cancer Amst. Neth.* **85**, 131–140 (2014).
943 43. Edelmann, M. *et al.* Cell cycle effects of radiation on human bronchial epithelium and lung carcinoma
944 cells in monolayer cultures and a three-dimensional co-culture system. *Radiat. Res.* **164**, 391–399
945 (2005).
946 44. Caldecott, K. W. Causes and consequences of DNA single-strand breaks. *Trends Biochem. Sci.* **49**, 68–
947 78 (2024).
948 45. Liao, H., Ji, F., Helleday, T. & Ying, S. Mechanisms for stalled replication fork stabilization: new targets
949 for synthetic lethality strategies in cancer treatments. *EMBO Rep.* **19**, e46263 (2018).
950 46. Balmus, G. *et al.* ATM orchestrates the DNA-damage response to counter toxic non-homologous end-
951 joining at broken replication forks. *Nat. Commun.* **10**, 87 (2019).
952 47. Takahashi, A. *et al.* Nonhomologous End-Joining Repair Plays a More Important Role than
953 Homologous Recombination Repair in Defining Radiosensitivity after Exposure to High-LET Radiation.
954 *Radiat. Res.* **182**, 338–344 (2014).
955 48. Kühne, M. *et al.* A Double-Strand Break Repair Defect in ATM-Deficient Cells Contributes to
956 Radiosensitivity. *Cancer Res.* **64**, 500–508 (2004).
957 49. Evan, G. & Littlewood, T. A Matter of Life and Cell Death. *Science* **281**, 1317–1322 (1998).
958 50. Williams, T. M., Yang, L., Estrada-Bernal, A., Chatterjee, M. & Robb, R. A KRAS-NRF2-53BP1
959 Nonhomologous End-Joining Repair Pathway Mediates Oncogenic KRAS Radioresistance. *Int. J.*
960 *Radiat. Oncol. Biol. Phys.* **99**, S31 (2017).
961 51. Larkin, J. *et al.* Combined Nivolumab and Ipilimumab or Monotherapy in Untreated Melanoma. *N.*
962 *Engl. J. Med.* **373**, 23–34 (2015).
963 52. Bozic, I. *et al.* Evolutionary dynamics of cancer in response to targeted combination therapy. *eLife* **2**,
964 e00747 (2013).
965 53. Baskar, R., Lee, K. A., Yeo, R. & Yeoh, K.-W. Cancer and Radiation Therapy: Current Advances and
966 Future Directions. *Int. J. Med. Sci.* **9**, 193–199 (2012).
967 54. Nair, N. U. *et al.* A landscape of response to drug combinations in non-small cell lung cancer. *Nat.*
968 *Commun.* **14**, 3830 (2023).
969 55. Yang, W. *et al.* Genomics of Drug Sensitivity in Cancer (GDSC): a resource for therapeutic biomarker
970 discovery in cancer cells. *Nucleic Acids Res.* **41**, D955-961 (2013).
971 56. Seashore-Ludlow, B. *et al.* Harnessing Connectivity in a Large-Scale Small-Molecule Sensitivity
972 Dataset. *Cancer Discov.* **5**, 1210–1223 (2015).
973 57. Corsello, S. M. *et al.* Discovering the anticancer potential of non-oncology drugs by systematic viability
974 profiling. *Nat. Cancer* **1**, 235–248 (2020).

975 58. Sinha, S. *et al.* PERCEPTION predicts patient response and resistance to treatment using single-cell
976 transcriptomics of their tumors. *Nat. Cancer* 1–15 (2024) doi:10.1038/s43018-024-00756-7.
977 59. Beaulieu, M.-E. *et al.* Intrinsic cell-penetrating activity propels Omomyc from proof of concept to
978 viable anti-MYC therapy. *Sci. Transl. Med.* **11**, eaar5012 (2019).
979 60. Llombart, V. & Mansour, M. R. Therapeutic targeting of 'undruggable' MYC. *EBioMedicine* **75**, 103756
980 (2022).
981 61. Peptomyc S.L. *A Phase 1/2 Study to Evaluate the Safety, Pharmacokinetics, and Anti-Tumour Activity*
982 *of the MYC Inhibitor OMO-103 Administered Intravenously in Patients With Advanced Solid Tumours*.
983 https://clinicaltrials.gov/study/NCT04808362 (2022).
984 62. Coker, E. A. *et al.* Individualized Prediction of Drug Response and Rational Combination Therapy in
985 NSCLC Using Artificial Intelligence–Enabled Studies of Acute Phosphoproteomic Changes. *Mol. Cancer*
986 *Ther.* **21**, 1020–1029 (2022).
987 63. Tolcher, A. W., Peng, W. & Calvo, E. Rational Approaches for Combination Therapy Strategies
988 Targeting the MAP Kinase Pathway in Solid Tumors. *Mol. Cancer Ther.* **17**, 3–16 (2018).
989 64. Poole, C. J. & van Riggelen, J. MYC—Master Regulator of the Cancer Epigenome and Transcriptome.
990 *Genes* **8**, 142 (2017).
991 65. Gabay, M., Li, Y. & Felsher, D. W. MYC Activation Is a Hallmark of Cancer Initiation and Maintenance.
992 *Cold Spring Harb. Perspect. Med.* **4**, (2014).
993 66. Soucek, L. *et al.* Inhibition of Myc family proteins eradicates KRas-driven lung cancer in mice. *Genes*
994 *Dev.* **27**, 504–513 (2013).
995 67. Savino, M. *et al.* The action mechanism of the Myc inhibitor termed Omomyc may give clues on how
996 to target Myc for cancer therapy. *PloS One* **6**, e22284 (2011).
997 68. Wang, C. *et al.* Alternative approaches to target Myc for cancer treatment. *Signal Transduct. Target.*
998 *Ther.* **6**, 1–14 (2021).
999 69. Garralda, E. *et al.* MYC targeting by OMO-103 in solid tumors: a phase 1 trial. *Nat. Med.* **30**, 762–771
1000 (2024).
1001 70. Luoto, K. R. *et al.* Tumor cell kill by c-MYC depletion: role of MYC-regulated genes that control DNA
1002 double-strand break repair. *Cancer Res.* **70**, 8748–8759 (2010).
1003 71. Vokes, N. I. *et al.* Concurrent TP53 Mutations Facilitate Resistance Evolution in EGFR-Mutant Lung
1004 Adenocarcinoma. *J. Thorac. Oncol.* **17**, 779–792 (2022).
1005 72. Hobor, S. *et al.* Mixed responses to targeted therapy driven by chromosomal instability through p53
1006 dysfunction and genome doubling. *Nat. Commun.* **15**, 4871 (2024).
1007 73. Cheng, G. *et al.* The tumor suppressor, p53, contributes to radiosensitivity of lung cancer cells by
1008 regulating autophagy and apoptosis. *Cancer Biother. Radiopharm.* **28**, 153–159 (2013).
1009 74. Gudkov, A. V. & Komarova, E. A. Pathologies Associated with the p53 Response. *Cold Spring Harb.*
1010 *Perspect. Biol.* **2**, a001180 (2010).
1011 75. Lee, C.-L., Blum, J. M. & Kirsch, D. G. Role of p53 in regulating tissue response to radiation by
1012 mechanisms independent of apoptosis. *Transl. Cancer Res.* **2**, 412–421 (2013).
1013 76. Stewart-Ornstein, J. *et al.* p53 dynamics vary between tissues and are linked with radiation sensitivity.
1014 *Nat. Commun.* **12**, 898 (2021).
1015 77. Zhang, J., Shen, L. & Sun, L.-Q. The regulation of radiosensitivity by p53 and its acetylation. *Cancer*
1016 *Lett.* **363**, 108–118 (2015).

1017 78. Hao, F., Gu, L. & Zhong, D. TP53 Mutation Mapping in Advanced Non-Small Cell Lung Cancer: A Real-
1018 World Retrospective Cohort Study. *Curr. Oncol.* **29**, 7411–7419 (2022).
1019 79. Chang, Y.-L., Wu, C.-T., Shih, J.-Y. & Lee, Y.-C. Comparison of p53 and epidermal growth factor receptor
1020 gene status between primary tumors and lymph node metastases in non-small cell lung cancers. *Ann.*
1021 *Surg. Oncol.* **18**, 543–550 (2011).
1022 80. Steeg, P. S. Tumor metastasis: mechanistic insights and clinical challenges. *Nat. Med.* **12**, 895–904
1023 (2006).
1024 81. Walls, G. M. *et al.* CONCORDE: A phase I platform study of novel agents in combination with
1025 conventional radiotherapy in non-small-cell lung cancer. *Clin. Transl. Radiat. Oncol.* **25**, 61–66 (2020).
1026 82. Dharia, N. V. *et al.* A first-generation pediatric cancer dependency map. *Nat. Genet.* **53**, 529–538
1027 (2021).
1028 83. Jaaks, P. *et al.* Effective drug combinations in breast, colon and pancreatic cancer cells. *Nature* **603**,
1029 166–173 (2022).
1030 84. Guo, C., Ma, X., Gao, F. & Guo, Y. Off-target effects in CRISPR/Cas9 gene editing. *Front. Bioeng.*
1031 *Biotechnol.* **11**, 1143157 (2023).
1032 85. Sheel, A. & Xue, W. Genomic amplifications cause false positives in CRISPR screens. *Cancer Discov.* **6**,
1033 824–826 (2016).
1034 86. Dede, M. & Hart, T. Recovering false negatives in CRISPR fitness screens with JLOE. *Nucleic Acids Res.*
1035 **51**, 1637–1651 (2023).
1036 87. Eduati, F. *et al.* Patient-specific logic models of signaling pathways from screenings on cancer biopsies
1037 to prioritize personalized combination therapies. *Mol. Syst. Biol.* **16**, e8664 (2020).
1038 88. Fröhlich, F. *et al.* Efficient Parameter Estimation Enables the Prediction of Drug Response Using a
1039 Mechanistic Pan-Cancer Pathway Model. *Cell Syst.* **7**, 567-579.e6 (2018).
1040 89. Fong, S. H. *et al.* A multilineage screen identifies actionable synthetic lethal interactions in human
1041 cancers. *Nat. Genet.* 1–11 (2024) doi:10.1038/s41588-024-01971-9.
1042 90. Cook, B., Fisher, J., Krepska, E. & Piterman, N. Proving Stabilization of Biological Systems. in
1043 *Verification, Model Checking, and Abstract Interpretation* (eds. Jhala, R. & Schmidt, D.) 134–149
1044 (Springer, Berlin, Heidelberg, 2011). doi:10.1007/978-3-642-18275-4_11.
1045 91. Zhu, Q. *et al.* Single cell multi-omics reveal intra-cell-line heterogeneity across human cancer cell lines.
1046 *Nat. Commun.* **14**, 8170 (2023).
1047 92. de Bruijn, I. *et al.* Analysis and Visualization of Longitudinal Genomic and Clinical Data from the AACR
1048 Project GENIE Biopharma Collaborative in cBioPortal. *Cancer Res.* **83**, 3861–3867 (2023).
1049 93. Yard, B. D. *et al.* A genetic basis for the variation in the vulnerability of cancer to DNA damage. *Nat.*
1050 *Commun.* **7**, 11428 (2016).
1051 94. Denz, R. & Timmesfeld, N. Visualizing the (Causal) Effect of a Continuous Variable on a Time-To-Event
1052 Outcome. *Epidemiol. Camb. Mass* **34**, 652–660 (2023).
1053 95. Benjamini, Y. & Hochberg, Y. Controlling the False Discovery Rate: A Practical and Powerful Approach
1054 to Multiple Testing. *J. R. Stat. Soc. Ser. B Methodol.* **57**, 289–300 (1995).
1055